

A11106 977920

NBS SPECIAL PUBLICATION **400-67**

U.S. DEPARTMENT OF COMMERCE / National Bureau of Standards

*Semiconductor Measurement Technology:*

The Capabilities and  
Limitations of Auger  
Sputter Profiling for  
Studies of Semiconductors

QC  
100  
J57  
NO. 400-67  
1981  
c. 2

# NATIONAL BUREAU OF STANDARDS

The National Bureau of Standards<sup>1</sup> was established by an act of Congress on March 3, 1901. The Bureau's overall goal is to strengthen and advance the Nation's science and technology and facilitate their effective application for public benefit. To this end, the Bureau conducts research and provides: (1) a basis for the Nation's physical measurement system, (2) scientific and technological services for industry and government, (3) a technical basis for equity in trade, and (4) technical services to promote public safety. The Bureau's technical work is performed by the National Measurement Laboratory, the National Engineering Laboratory, and the Institute for Computer Sciences and Technology.

**THE NATIONAL MEASUREMENT LABORATORY** provides the national system of physical and chemical and materials measurement; coordinates the system with measurement systems of other nations and furnishes essential services leading to accurate and uniform physical and chemical measurement throughout the Nation's scientific community, industry, and commerce; conducts materials research leading to improved methods of measurement, standards, and data on the properties of materials needed by industry, commerce, educational institutions, and Government; provides advisory and research services to other Government agencies; develops, produces, and distributes Standard Reference Materials; and provides calibration services. The Laboratory consists of the following centers:

Absolute Physical Quantities<sup>2</sup> — Radiation Research — Thermodynamics and Molecular Science — Analytical Chemistry — Materials Science.

**THE NATIONAL ENGINEERING LABORATORY** provides technology and technical services to the public and private sectors to address national needs and to solve national problems; conducts research in engineering and applied science in support of these efforts; builds and maintains competence in the necessary disciplines required to carry out this research and technical service; develops engineering data and measurement capabilities; provides engineering measurement traceability services; develops test methods and proposes engineering standards and code changes; develops and proposes new engineering practices; and develops and improves mechanisms to transfer results of its research to the ultimate user. The Laboratory consists of the following centers:

Applied Mathematics — Electronics and Electrical Engineering<sup>2</sup> — Mechanical Engineering and Process Technology<sup>2</sup> — Building Technology — Fire Research — Consumer Product Technology — Field Methods.

**THE INSTITUTE FOR COMPUTER SCIENCES AND TECHNOLOGY** conducts research and provides scientific and technical services to aid Federal agencies in the selection, acquisition, application, and use of computer technology to improve effectiveness and economy in Government operations in accordance with Public Law 89-306 (40 U.S.C. 759), relevant Executive Orders, and other directives; carries out this mission by managing the Federal Information Processing Standards Program, developing Federal ADP standards guidelines, and managing Federal participation in ADP voluntary standardization activities; provides scientific and technological advisory services and assistance to Federal agencies; and provides the technical foundation for computer-related policies of the Federal Government. The Institute consists of the following centers:

Programming Science and Technology — Computer Systems Engineering.

<sup>1</sup>Headquarters and Laboratories at Gaithersburg, MD, unless otherwise noted; mailing address Washington, DC 20234.

<sup>2</sup>Some divisions within the center are located at Boulder, CO 80303.

1940 - 1941  
1942  
1943  
1944  
1945  
1946  
1947  
1948  
1949  
1950  
1951  
1952  
1953  
1954  
1955  
1956  
1957  
1958  
1959  
1960  
1961  
1962  
1963  
1964  
1965  
1966  
1967  
1968  
1969  
1970  
1971  
1972  
1973  
1974  
1975  
1976  
1977  
1978  
1979  
1980  
1981  
1982  
1983  
1984  
1985  
1986  
1987  
1988  
1989  
1990  
1991  
1992  
1993  
1994  
1995  
1996  
1997  
1998  
1999  
2000  
2001  
2002  
2003  
2004  
2005  
2006  
2007  
2008  
2009  
2010  
2011  
2012  
2013  
2014  
2015  
2016  
2017  
2018  
2019  
2020  
2021  
2022  
2023  
2024  
2025  
2026  
2027  
2028  
2029  
2030  
2031  
2032  
2033  
2034  
2035  
2036  
2037  
2038  
2039  
2040  
2041  
2042  
2043  
2044  
2045  
2046  
2047  
2048  
2049  
2050  
2051  
2052  
2053  
2054  
2055  
2056  
2057  
2058  
2059  
2060  
2061  
2062  
2063  
2064  
2065  
2066  
2067  
2068  
2069  
2070  
2071  
2072  
2073  
2074  
2075  
2076  
2077  
2078  
2079  
2080  
2081  
2082  
2083  
2084  
2085  
2086  
2087  
2088  
2089  
2090  
2091  
2092  
2093  
2094  
2095  
2096  
2097  
2098  
2099  
2100  
2101  
2102  
2103  
2104  
2105  
2106  
2107  
2108  
2109  
2110  
2111  
2112  
2113  
2114  
2115  
2116  
2117  
2118  
2119  
2120  
2121  
2122  
2123  
2124  
2125  
2126  
2127  
2128  
2129  
2130  
2131  
2132  
2133  
2134  
2135  
2136  
2137  
2138  
2139  
2140  
2141  
2142  
2143  
2144  
2145  
2146  
2147  
2148  
2149  
2150  
2151  
2152  
2153  
2154  
2155  
2156  
2157  
2158  
2159  
2160  
2161  
2162  
2163  
2164  
2165  
2166  
2167  
2168  
2169  
2170  
2171  
2172  
2173  
2174  
2175  
2176  
2177  
2178  
2179  
2180  
2181  
2182  
2183  
2184  
2185  
2186  
2187  
2188  
2189  
2190  
2191  
2192  
2193  
2194  
2195  
2196  
2197  
2198  
2199  
2200  
2201  
2202  
2203  
2204  
2205  
2206  
2207  
2208  
2209  
2210  
2211  
2212  
2213  
2214  
2215  
2216  
2217  
2218  
2219  
2220  
2221  
2222  
2223  
2224  
2225  
2226  
2227  
2228  
2229  
2230  
2231  
2232  
2233  
2234  
2235  
2236  
2237  
2238  
2239  
2240  
2241  
2242  
2243  
2244  
2245  
2246  
2247  
2248  
2249  
2250  
2251  
2252  
2253  
2254  
2255  
2256  
2257  
2258  
2259  
2260  
2261  
2262  
2263  
2264  
2265  
2266  
2267  
2268  
2269  
2270  
2271  
2272  
2273  
2274  
2275  
2276  
2277  
2278  
2279  
2280  
2281  
2282  
2283  
2284  
2285  
2286  
2287  
2288  
2289  
2290  
2291  
2292  
2293  
2294  
2295  
2296  
2297  
2298  
2299  
2300  
2301  
2302  
2303  
2304  
2305  
2306  
2307  
2308  
2309  
2310  
2311  
2312  
2313  
2314  
2315  
2316  
2317  
2318  
2319  
2320  
2321  
2322  
2323  
2324  
2325  
2326  
2327  
2328  
2329  
2330  
2331  
2332  
2333  
2334  
2335  
2336  
2337  
2338  
2339  
2340  
2341  
2342  
2343  
2344  
2345  
2346  
2347  
2348  
2349  
2350  
2351  
2352  
2353  
2354  
2355  
2356  
2357  
2358  
2359  
2360  
2361  
2362  
2363  
2364  
2365  
2366  
2367  
2368  
2369  
2370  
2371  
2372  
2373  
2374  
2375  
2376  
2377  
2378  
2379  
2380  
2381  
2382  
2383  
2384  
2385  
2386  
2387  
2388  
2389  
2390  
2391  
2392  
2393  
2394  
2395  
2396  
2397  
2398  
2399  
2400  
2401  
2402  
2403  
2404  
2405  
2406  
2407  
2408  
2409  
2410  
2411  
2412  
2413  
2414  
2415  
2416  
2417  
2418  
2419  
2420  
2421  
2422  
2423  
2424  
2425  
2426  
2427  
2428  
2429  
2430  
2431  
2432  
2433  
2434  
2435  
2436  
2437  
2438  
2439  
2440  
2441  
2442  
2443  
2444  
2445  
2446  
2447  
2448  
2449  
2450  
2451  
2452  
2453  
2454  
2455  
2456  
2457  
2458  
2459  
2460  
2461  
2462  
2463  
2464  
2465  
2466  
2467  
2468  
2469  
2470  
2471  
2472  
2473  
2474  
2475  
2476  
2477  
2478  
2479  
2480  
2481  
2482  
2483  
2484  
2485  
2486  
2487  
2488  
2489  
2490  
2491  
2492  
2493  
2494  
2495  
2496  
2497  
2498  
2499  
2500  
2501  
2502  
2503  
2504  
2505  
2506  
2507  
2508  
2509  
2510  
2511  
2512  
2513  
2514  
2515  
2516  
2517  
2518  
2519  
2520  
2521  
2522  
2523  
2524  
2525  
2526  
2527  
2528  
2529  
2530  
2531  
2532  
2533  
2534  
2535  
2536  
2537  
2538  
2539  
2540  
2541  
2542  
2543  
2544  
2545  
2546  
2547  
2548  
2549  
2550  
2551  
2552  
2553  
2554  
2555  
2556  
2557  
2558  
2559  
2560  
2561  
2562  
2563  
2564  
2565  
2566  
2567  
2568  
2569  
2570  
2571  
2572  
2573  
2574  
2575  
2576  
2577  
2578  
2579  
2580  
2581  
2582  
2583  
2584  
2585  
2586  
2587  
2588  
2589  
2590  
2591  
2592  
2593  
2594  
2595  
2596  
2597  
2598  
2599  
2600  
2601  
2602  
2603  
2604  
2605  
2606  
2607  
2608  
2609  
2610  
2611  
2612  
2613  
2614  
2615  
2616  
2617  
2618  
2619  
2620  
2621  
26

# The Capabilities and Limitations of Auger Sputter Profiling for Studies of Semiconductors

Stanford Electronics Laboratories  
Electrical Engineering Department  
Stanford University  
Stanford, CA 94305

and

N. J. Taylor

Varian Associates  
611 Hansen Way  
Palo Alto, CA 94303

Sponsored by the

Defense Advanced Research Projects Agency  
1400 Wilson Boulevard  
Arlington, VA 22203



U.S. DEPARTMENT OF COMMERCE, Malcolm Baldrige, Secretary  
NATIONAL BUREAU OF STANDARDS, Ernest Ambler, Director

Issued September 1981

Library of Congress Catalog Card Number: 81-600003

National Bureau of Standards Special Publication 400-67

Nat. Bur. Stand. (U.S.), Spec. Publ. 400-67, 53 pages (Sept. 1981)

CODEN: XNBSAV

U.S. GOVERNMENT PRINTING OFFICE

WASHINGTON: 1981

---

# TABLE OF CONTENTS

	Page
Abstract . . . . .	1
1. Introduction . . . . .	2
2. Basic Equipment . . . . .	2
2.1 Electron Spectrometer and Electron Gun . . . . .	2
2.2 The Ion Gun . . . . .	3
2.3 The Specimen Holder . . . . .	4
3. Sensitivity and Spatial Resolution . . . . .	4
4. Electron Escape Depth Broadening . . . . .	6
4.1 Introduction . . . . .	6
4.2 The Electron Mean Free Path . . . . .	7
4.3 A Deconvolution Formula . . . . .	8
4.4 Off-Normal Detection . . . . .	10
4.5 Surface Roughness and Experimental Nonlinearities . . . . .	14
5. Ion Bombardment Effects . . . . .	15
5.1 Introduction . . . . .	15
5.2 Atomic Interactions . . . . .	16
5.2.1 Introduction . . . . .	16
5.2.2 Nuclear Energy Loss . . . . .	16
5.2.3 Electronic Energy Loss . . . . .	20
5.2.4 Atomic Displacements . . . . .	21
5.2.5 Summary . . . . .	21
5.3 A Geometrical Model of Sputtering . . . . .	21
5.3.1 Introduction . . . . .	21
5.3.2 Development . . . . .	22
5.3.3 Computation . . . . .	25
5.3.4 Experimental Comparisons . . . . .	25
5.3.5 Discussion . . . . .	29
5.3.6 Summary . . . . .	32
5.4 An Ion Knock-On Mixing Model . . . . .	32
5.4.1 Introduction . . . . .	32
5.4.2 Development . . . . .	32
5.4.3 Experiment . . . . .	33
5.4.4 Extension to Higher Energies . . . . .	34
5.4.5 Summary . . . . .	37
6. Experimental Methods in ASP Studies of the Si-SiO <sub>2</sub> Interface . . . . .	38
6.1 Introduction . . . . .	38
6.2 Experimental Suppression of Profile Broadening . . . . .	38
6.3 Electron Stimulated Desorption . . . . .	39
6.4 Experimental Procedure . . . . .	41
6.5 Crater-Edge Profiling . . . . .	42
6.6 Experimental Results for the Width of the Si-SiO <sub>2</sub> Interface . . . . .	43
References . . . . .	44

# LIST OF ILLUSTRATIONS

	Page
1. Typical beam diameter versus beam current with $\text{LaB}_6$ emitter--solid curve . . . .	6
2. Maximum sensitivity of AES as a function of electron beam diameter . . . . .	7
3. Experimentally observed variations of the electron escape depth as a function of the electron energy . . . . .	8
4. Effect of escape depth broadening on a step function concentration profile . . .	10
5. Electron escape depths for Si and $\text{SiO}_2$ as a function of electron energy . . . . .	12
6. Auger depth profile of the oxygen concentration in an MNOS sample . . . . .	12
7. Auger sputter profile of thermally grown Si- $\text{SiO}_2$ interface . . . . .	13
8. An Auger sputter profile of the Si- $\text{SiO}_2$ interface is deconvolved through the use of Eq. (10) in the text . . . . .	13
9. Four situations yielding equivalent measured profiles . . . . .	14
10. The 10% to 90% width $\Delta y_1$ and 50% position shift $\Delta y_2$ as a function of the roughness parameter $\Delta x$ . . . . .	15
11. Schematic illustration of the sputtering and mixing processes resulting from ion bombardment . . . . .	16
12. (a) A particle of mass $M_1$ approaches and deflects an initially stationary particle $M_2$ . (b) These particles are modeled as billiard balls with adjus- table radii . . . . .	17
13. Reduced stopping power as a function of reduced energy for the Thomas-Fermi potential, the inverse square potential, and for electronic energy loss . . . . .	19
14. Reduced range versus reduced energy for the Thomas-Fermi potential and the inverse square potential . . . . .	19
15. Definition of ellipsoid parameters and cross-sectional areas . . . . .	23
16. Illustration of the sputtering yield variation with ion energy . . . . .	26
17. The relative sputtering yield is plotted as a function of the nuclear energy loss $E$ for several values of $\beta$ . . . . .	26
18. Sputtering yields of Ag versus ion energy for $\text{Xe}^+$ , $\text{Kr}^+$ , $\text{Ar}^+$ , and $\text{Ne}^+$ ions at normal incidence . . . . .	27
19. The surface factor $B$ derived from Rosenberg and Wehner is plotted as a function of atomic number $Z$ . . . . .	28
20. The surface factor $B$ is divided by the square root of the atomic mass and plotted in relation to the periodic table for the transition metals . . . . .	28
21. Sputtering yields of Au bombarded by 45-keV ions normalized to $\text{Ar}^+$ yield . . . .	29
22. Pictorial representation of the sputtering yields angular dependence . . . . .	30
23. Sputtering yield ratios at normal and $50^\circ$ incidence versus $\text{Ar}^+$ ion energy; experimental and theoretical . . . . .	30



# ILLUSTRATIONS (continued)

	Page
24. Relative sputtering yield increases as a function of incident angle; experimental and theoretical . . . . .	31
25. Schematic illustration of a random walk with $N$ steps of length $a_1$ and a net distance traveled $R$ . . . . .	34
26. A step function concentration profile is broadened by ion knock-on mixing into an erf profile with a 10% to 90% width of 3.6 $W$ . . . . .	34
27. Average and standard deviation of sputtering yields in thermal $\text{SiO}_2$ as a function of ion energy for $\text{Ne}^+$ , $\text{Ar}^+$ , and $\text{Xe}^+$ bombardment . . . . .	34
28. Average and standard deviation of the measured 10% to 90% $\text{Si-SiO}_2$ interface widths as a function of ion energy for $\text{Ne}^+$ , $\text{Ar}^+$ , and $\text{Xe}^+$ bombardment . . . . .	35
29. The effect of ESD on the $\text{O}_{\text{KLL}}$ and $\text{Si}_{\text{LVV}}$ lines from $\text{SiO}_2$ and $\text{SiO}_x$ shown as a function of irradiation time for an electron beam flux larger than $2 \times 10^{17} \text{ cm}^{-2} \text{ s}^{-1}$ at 2 keV . . . . .	39
30. The total desorption cross section of oxygen at 2 keV shown as a function of primary flux for a silicon oxide . . . . .	40
31. The upper part shows the dependence of the cross section on primary electron energy; the lower part shows how the secondary electron density depends on primary electron energy . . . . .	41
32. Schematic illustration of the crater formed by sputtering a thin layer of $\text{SiO}_2$ on $\text{Si}$ . . . . .	42
33. Sequential $\text{Si}_{\text{LVV}}$ spectra obtained while sputtering through the $\text{Si-SiO}_2$ interface . . . . .	43

## LIST OF TABLES

	Page
1. Maximum Estimated AES Sensitivities . . . . .	5
2. Values of Surface Factor $B$ . . . . .	27
3. Comparison of Monte Carlo Calculations of the Broadening Induced by $\text{Ar}^+$ Bombardment of $\text{Si}$ with the Predictions of the Present Model . . . . .	36
4. Oxide Thickness Dependence of the Width of the $\text{Si-SiO}_2$ Transition Region . . . . .	43

## PREFACE

This study was carried out at Stanford University and Varian Associates as a part of the Semiconductor Technology Program in the Electron Devices Division at the National Bureau of Standards. The Semiconductor Technology Program serves to focus NBS efforts to enhance the performance, interchangeability, and reliability of discrete semiconductor devices and integrated circuits through improvements in measurement technology for use in specifying materials and devices in national and international commerce and for use by industry in controlling device fabrication processes. The work was supported by the Defense Advanced Research Projects Agency, ARPA Order 2397, through the National Bureau of Standards' Semiconductor Technology Program, Contract 5-35944. This contract was monitored by Dr. K. F. Galloway as the Contracting Officer's Technical Representative. Dr. W. M. Bullis provided technical review of this report for the National Bureau of Standards.

## Disclaimer

Certain commercially available equipment, instruments, or materials are identified in this publication in order to adequately specify the experimental procedure. Such identification does not imply recommendation or endorsement by the National Bureau of Standards, nor does it imply that the materials or equipment identified are necessarily the best available for the purpose.



*Semiconductor Measurement Technology:*  
The Capabilities and Limitations of Auger Sputter  
Profiling for Studies of Semiconductors

by

S. A. Schwarz, C. R. Helms, and W. E. Spicer  
Stanford Electronics Laboratories  
Electrical Engineering Department  
Stanford University  
Stanford, California 94305

and

N. J. Taylor  
Varian Associates  
Palo Alto, California 94303

Abstract

Materials characterization is a critical area in current silicon integrated circuit technology. Those techniques that are commonly used include Auger sputter profiling, x-ray photoelectron spectroscopy, secondary ion mass spectrometry, and Rutherford backscattering. All of these techniques have unique capabilities and limitations for studies of silicon device structures. In this paper, we describe the capabilities and limitations of Auger sputter profiling especially with regard to sensitivity, spatial resolution, depth resolution, and chemical state determination. Although much of the discussion centers on Auger sputter profiling, the results are also applicable to x-ray photoelectron spectroscopy and secondary ion mass spectrometry.

*Key words:* Auger electron spectroscopy (AES); metal-oxide-semiconductor (MOS); secondary ion mass spectrometry (SIMS); semiconductor devices; sputtering; x-ray photoelectron spectroscopy (XPS, ESCA).

## 1. INTRODUCTION

The purpose of this report is to provide critical information concerning the use of electron spectroscopy and ion milling for the analysis of materials used in silicon integrated circuit technology. The emphasis of this report is placed on Auger electron spectroscopy (AES); however, many of the results are also applicable to x-ray photoelectron spectroscopy (XPS) and secondary ion mass spectrometry (SIMS). We concentrate on the use of these techniques to obtain elemental profiles perpendicular to the surface of a specimen of interest in IC technology. In addition to elemental profiles, the use of AES to perform chemical state (i.e., the difference between Si in bulk Si vs Si in SiO<sub>2</sub>) determination is also discussed. Most of the discussion centers on effects important in Si and SiO<sub>2</sub>, although it is not limited to those materials alone.

This paper is divided into six sections. After the Introduction, Section 2 contains a brief description of modern equipment used for Auger sputter profiling (ASP). Next, in Section 3, the sensitivity and spatial resolution are discussed. In Section 4, the effect of electron escape depth, in particular, the broadening it produces during profiling, is discussed. The ion beam used for profiling also causes knock-on induced broadening; these effects are discussed in Section 5. Finally, Section 6 covers the application of Auger sputter profiling to studies of the Si-SiO<sub>2</sub> interface, including the use of AES to determine the chemical state of elements and the effect of electron stimulated desorption.

## 2. BASIC EQUIPMENT

### 2.1 Electron Spectrometer and Electron Gun

Because of the commercial availability of cylindrical mirror analyzers (with integral electron guns) and because most depth profiling has been carried out using them to date, we shall specifically consider this type of analyzer and gun. Other types of analyzers could be used, however, bearing in mind the desirability of a large angle of acceptance (for signal-to-noise considerations) and adequate separation between the specimen and analyzer to accommodate the ion beam without danger of sputtering material from the analyzer or the electron gun onto the specimen.

The electron beam should be capable of being focused onto the region of the specimen of interest located at the focal point of the analyzer. In most general studies on patternless thin films, a minimum electron beam diameter of from 10 to 30  $\mu\text{m}$  is adequate. This is the kind of film we shall be considering here for the most part. The profiling of actual circuits may require beams of diameter down to and below 1  $\mu\text{m}$ , depending upon the region to be profiled. In these cases, the effects of the geometrical constraints are obviously more severe than those we are considering here. Nevertheless, the same principles apply. In high spatial resolution cases, it may even develop that the information cannot be found because of an unfavorable signal-to-noise/specimen damage tradeoff imposed by the small specimen, as discussed in the next section.

For an electron beam diameter in the range of 10 to 30  $\mu\text{m}$ , beam currents in the range of 1 to 100  $\mu\text{A}$  are desirable. To avoid electron beam-induced dissociation and desorption effects, particularly of oxides, reduced exposure is required during the acquisition of data. This means that in order to obtain adequate signal-to-noise ratio, it may be necessary to increase the area from which the information is acquired. Uniform exposure over the acceptance area of the analyzer is best accomplished by scanning the electron beam over the focal region of the analyzer. This can be accomplished by using a TV raster of the electron beam over the specimen surface. Provided this raster is kept less than about 200  $\mu\text{m}$  on an edge, the Auger signal is not seriously affected by the rastering since the raster falls inside the 90% signal contour of the typical analyzer.

Another requirement of the electron beam, in addition to its being rastered (both for density reduction and image specimen capability), is that it be capable of being deflected

on the specimen in a dc manner for centering at the focal point of the analyzer. The latter is required for "crater-edge profiling" [1]. The beam current should also be capable of being readily measured and adjusted and held reasonably constant over the time required for a typical profile (5 min to 1 hr).

To date, most profiling has been done in "static" vacuum systems. Such a system is first pumped down with sorption, sputter-ion, and titanium sublimation pumps (TSP) (sometimes after bakeout for ~8 hr at 250°C) to a base pressure of about  $10^{-10}$  Torr. Fresh titanium is then sublimed onto the pumping chamber walls, the ion pump is turned off, and an inert sputtering gas such as argon is introduced, typically to a pressure of  $10^{-5}$  to  $5 \times 10^{-5}$  Torr. The fresh titanium keeps the active-gas partial pressure many orders of magnitude below that of the inert sputtering gas. The methane level may rise, however, after a period of 30 min or so to two orders of magnitude below that of the argon, and the pressure of carbon monoxide will rise to a lesser degree. Their effect on the profiling, in which usually at least ten atomic layers per minute are being removed, is almost always negligible. The introduction of argon has two main effects on the electron gun. Some of the argon is ionized by the electron beam within the electron gun, and while the loss of electrons from the beam is negligible, the positive ions within the gun cause a perturbation in the electric fields, requiring a readjustment of the lenses to approximate the original beam. Some ions are also accelerated towards the filament, sputter cleaning it (and perhaps changing the electron emission) and, of course, eroding it. If the filament current is held constant, there will then be a higher temperature and thus higher evaporation at the eroded region, thereby hastening failure. The filament should therefore be conservatively operated as much as possible to maintain its lifetime. This means keeping the filament temperature as low as possible, consistent with adequate beam current. Thus, during the life of the filament, the filament current should be progressively reduced to attempt to maintain constant temperature at the eroded center. Obviously, it is difficult to prescribe any detailed steps. The user, knowing principles of the mechanism of filament failure, however, can in a gross sense, take broad steps to prolonging filament life. The condition of the filament can be checked, for example, by measuring the anode current at a given beam energy and filament current with minimum Wehnelt (extractor) bias. The filament current may then be reduced accordingly.

In dynamic systems, filament sputtering is greatly reduced. In such a system, the sputtering gas is introduced into the ionizer of the ion gun, and the system is then held at a pressure several orders of magnitude less than that in the ionizer by the use of a restrictive aperture in the ion gun. Such guns differ from most of those that have been used to date in that two lenses (instead of the single lens) in addition to the source lens are used. The restrictive aperture is conveniently located at the beam crossover after the first lens. In this case, the inert gas is continuously leaked into the ionizer to compensate for that pumped by the system pump.

## 2.2 The Ion Gun

The purpose of the ion gun is, of course, to produce an ion beam usually of inert gas ions (Ar, Xe, Ne, Kr) of suitable energy and density and of sufficient cross-sectional size and uniformity to uniformly sputter-etch away (in ideal cases) thin surface films. Most films studied lie in the range of from a few Angstroms to  $1 \mu\text{m}$  thick. The ion gun should be capable of producing ion-beam current densities of several hundred microamps per square centimeter, and the energy range of the ions should be controllable from a few hundred to a few thousand electronvolts. At the higher energies and current densities, the sputtering rate for most materials lies in the range of from 10 to 50 nm/min. Thus, the sputtering time for a  $1 \mu\text{m}$  thick film is 100 to 20 min. The factors determining the choice of energy and rate are discussed in later sections.

Most of the ion guns used to date in conjunction with Auger spectrometers have had purely electrostatic ionization regions in which the ionization has been created by electrons accelerated to about 200 eV from a hot filament. A suitable extraction region, often gridded, helps form a beam which is subsequently focused and deflected electrostatically. In guns of this type, an optimum pressure in the ionization region lies between  $10^{-5}$  and  $10^{-4}$  Torr. As mentioned earlier, in "static" systems, the whole system is brought to this pressure after turning off the ion pump. All of the experience reported here is in



systems of this type. The operational difference between this and the differentially pumped ion gun arrangement would be expected to be in the lower residual gas level in the latter case and, as mentioned previously, the improvement in filament life. The deflection plates are necessary to bring the center of the ion beam to the focal point of the analyzer, at which point the electron beam is directed. Poor positioning results in poor depth resolution. Rastering should also be provided on the deflection plates. This serves two functions:

- (1) It provides a flatter crater bottom by smearing out the small variations in intensity created near the beam center by both nonuniform ionization and, in some cases, the inadvertent "imaging" of the transverse extraction grid (in guns with such a grid). The falloff diameter is also extended by the rastering, thereby providing flatness over a wider area. This is of particular importance when it is necessary to also raster the electron beam because of electron beam damage effects.
- (2) It provides a convenient control over the ion beam current density. It is useful to be able to reduce the beam current density to a predetermined level by increasing the raster a chosen amount as an interface is approached. This enables more data points or improved signal-to-noise to be obtained in the vicinity of the interface.

### 2.3 The Specimen Holder

Carousel specimen holders have been extensively used in depth profiling. One station of the carousel should contain a Faraday cup with which a number of important measurements and setup procedures can be carried out. The specimens should be held firmly to the holder or tray using suitable springs.

From observation of the aperture of the Faraday cup using the electron beam raster, it is possible to first bring one side of the periphery of the aperture to the focal point of the analyzer. This is done by reducing the raster to zero, setting the beam energy to 2 keV, and then observing the elastic peak at 2 keV and optimizing it through translation along the axis such that its intensity is maximized. The raster is then restored and the Faraday cup translated horizontally, perpendicular to the analyzer axis, until the aperture is centered at the center of the raster--the focal point of the analyzer. This aperture can now be used to position the ion beam by maximizing the ion beam current into the cup using the deflection and focus controls of the ion gun.

From the aperture dimensions (including its thickness) and the angle between the aperture and the ion beam axis, the ion beam current density (in the axial direction) can be measured. The sputtering rate for a particular specimen is proportional to this density and a function of ion beam energy and angle. If the angle between the ion beam and the specimen surface is increased, the actual current density at the surface is reduced as the cosecant of the angle. To a certain degree, this reduction in ion beam density is compensated for by a corresponding increase in sputtering rate.

If the ion gun is rastered, the Faraday cup can also be used to measure the ion beam current density distribution by translating the cup horizontally and vertically and recording the current into the cup as a function of position. For small amounts of movement, e.g.,  $\pm 3$  mm, the effect of the change in angle subtended by the aperture at the exit of the gun usually can be neglected.

## 3. SENSITIVITY AND SPATIAL RESOLUTION

Questions of sensitivity and spatial resolution in AES must be dealt with together since, for a constant brightness source, an increase in spatial resolution can only be achieved through a reduction in beam current and therefore a loss in sensitivity for a

given data collection time. By spatial resolution, we mean the dimensions parallel to the surface of the sample; the resolution perpendicular to the specimen's surface is determined by the escape depth which is discussed in the following section. In order to ensure that the analysis of this section has the most general applicability, figures for source brightness and signal-to-noise ratio will be taken from currently available commercial equipment. In addition to the interdependence of these two factors, electron beam-induced damage will also affect sensitivity and spatial resolution limits. One such effect is electron stimulated desorption of oxygen from  $\text{SiO}_2$ , which is discussed in more detail in Section 6.3.

In order to discuss sensitivity, we will consider a baseline case with the following parameters: lock-in amplifier detection system providing an output of  $d(E \cdot N(E))/dE$ , where  $E$  is energy and  $N(E)$  is the distribution of electrons, 100  $\mu\text{A}$  beam current, 2.4% analyzer resolution, 30 min data collection time, 10 V peak-to-peak modulation voltage, 50 V scan, and signal averaging using a multichannel analyzer or minicomputer.

In general, the signal-to-noise ratio is given by

$$\frac{S}{N} = A\sqrt{It} \left(\frac{\Delta E}{E}\right)^{1/2} V_{\text{ptp}} \quad (1)$$

where  $A$  is a constant,  $I$  is the beam current,  $(\Delta E/E)$  is the resolution of the analyzer,  $t$  is time, and  $V_{\text{ptp}}$  is the modulation voltage. This assumes that the value of  $\Delta E/E$  chosen, as well as  $V_{\text{ptp}}$ , do not contribute any broadening to the line shape which limits both  $V_{\text{ptp}}$  and  $\Delta E$  to 5 eV for most transitions. Also, the  $\sqrt{t}$  dependence can only be realized for random noise and can be significantly affected by any coherent noise present. Within these assumptions, we will define the maximum AES sensitivity as the concentration of the element with the strongest Auger transition for which  $S/N = 1$ .

Remarkable as it may seem, no measurements of this maximum sensitivity are available. From extrapolating data taken at much less ideal conditions, a value for the maximum sensitivity of AES of  $\sim 10^{17} \text{ cm}^{-3}$  can be estimated. This value of maximum sensitivity, however, does not correspond to all elements, but to the maximum strength AES transitions such as the Ag MNN transition or the Cl LMM transition. Maximum sensitivities for other elements of interest are listed in Table 1, within  $\pm$  half order of magnitude. These values are based on the assumption that there are no interference effects from neighboring transitions.

Table 1

MAXIMUM ESTIMATED AES SENSITIVITIES

Element	Sensitivity	Comments
B	$10^{18} \text{ cm}^{-3}$	Ar interference
C	$3 \times 10^{17} \text{ cm}^{-3}$	background contamination
N	$3 \times 10^{17} \text{ cm}^{-3}$	---
O	$3 \times 10^{17} \text{ cm}^{-3}$	background contamination
F	$3 \times 10^{17} \text{ cm}^{-3}$	---
Na	$10^{18} \text{ cm}^{-3}$	beam-induced drift
Al	$3 \times 10^{17} \text{ cm}^{-3}$	Si interference
Si	$3 \times 10^{17} \text{ cm}^{-3}$	---
P	$3 \times 10^{17} \text{ cm}^{-3}$	Si interference
Cl	$10^{17} \text{ cm}^{-3}$	Ar interference
As	$3 \times 10^{18} \text{ cm}^{-3}$	---
Sb	$10^{17} \text{ cm}^{-3}$	---

To obtain these sensitivities within a 30-min data collection time, a 100  $\mu\text{A}$  beam current would be required. Presently, typical guns with  $\text{LaB}_6$  emitters can provide this beam current with a minimum spot size of less than 10  $\mu\text{m}$  in diameter. This corresponds to a current density of 100  $\text{A}/\text{cm}^2$ , a power density of  $5 \times 10^5 \text{ W}/\text{cm}^2$ , and a total power dissipation of  $\sim 1/2 \text{ W}$ . These levels are sufficient to cause local melting of silicon under typical conditions. To bring beam effects to acceptable levels under these conditions, rastering the electron beam over a  $100 \times 100$  to  $200 \times 200 \mu\text{m}$  area is required. Typical values for beam diameter versus beam current are shown in Fig. 1 as the solid curve; the dashed curve is the maximum current versus beam size to ensure that no significant damage is occurring in Si. In Fig. 2, the variation of maximum sensitivity of AES as a function of beam diameter is presented. The solid curve is for Si; the two dashed curves represent the limit in  $\text{SiO}_2$  for beam energies of 4.5 keV with the indicated amounts of elemental silicon present in the spectrum due to electron stimulated desorption. It should be stressed at this point that much instrumentation exists in the field today that does not possess the capabilities mentioned above. For example, instruments with beam currents of 10  $\mu\text{A}$ , 0.3% analyzer resolutions, and without minicomputer facilities, are common. In this case, a factor of 10 degradation in sensitivity is probable.

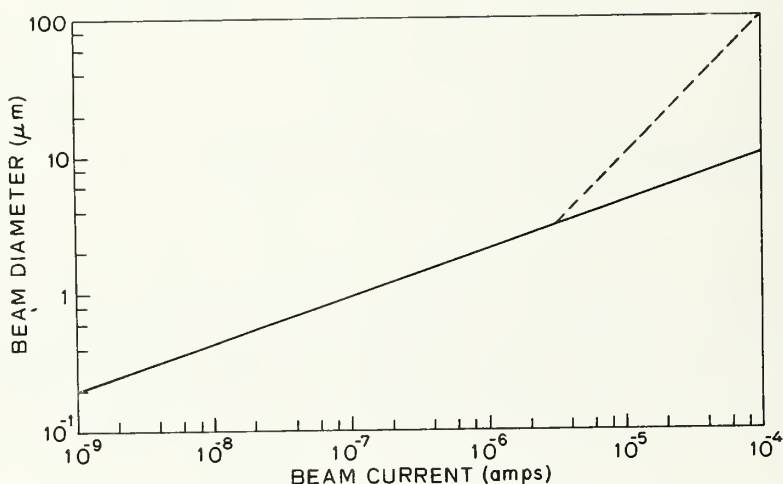


Fig. 1. Typical beam diameter versus beam current with  $\text{LaB}_6$  emitter--solid curve. Dashed segment corresponds to the approximate increase in beam size necessary to keep the local sample temperature down to reasonable levels in silicon.

#### 4. ELECTRON ESCAPE DEPTH BROADENING

##### 4.1 Introduction

Auger electrons lose energy via several scattering mechanisms before escaping into vacuum at the specimen surface. If this energy loss is significant, the Auger electron no longer has an energy characteristic of the element from which it came. The electron escape depth  $L$  is defined as the mean free path between "lossy" scattering events. The majority of Auger electrons generated within a distance  $L$  from the surface escape without significant energy loss. In an Auger sputter profiling (ASP) experiment, the measured elemental signal strength represents an average concentration in the surface region of thickness  $\sim L$ . Thus, the depth resolution of ASP is limited by the escape depth.



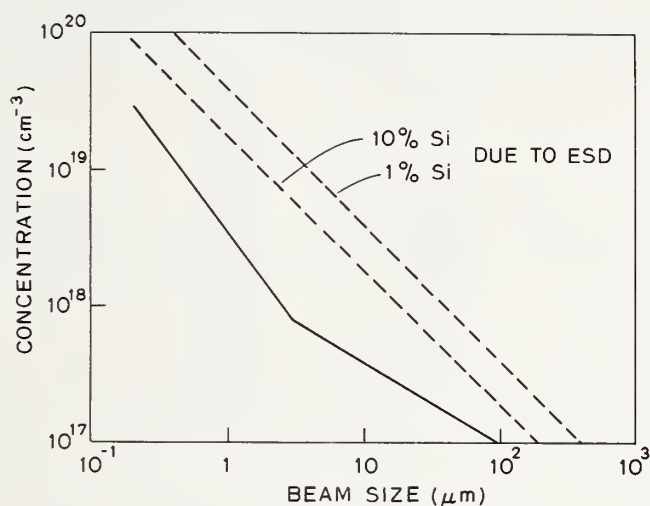


Fig. 2. Maximum sensitivity of AES (to chlorine or silver transitions) as a function of electron beam diameter. Solid curve derived from Fig. 1. Dashed curves correspond to the degradation in sensitivity in  $\text{SiO}_2$  due to electron stimulated desorption esd. The 10% and 1% Si curves correspond to beam size and sensitivity such that the spectra will contain 10% or 1% contribution from elemental silicon due to esd.

Electron escape depth broadening is examined in the following sections. In Section 4.2, the energy and substrate dependence of  $L$  is briefly discussed. In Section 4.3, we derive a simple formula which allows for the deconvolution of electron escape depth broadening from the measured profile. An appropriate deconvolution formula for a cylindrical mirror analyzer (CMA) detector is derived in Section 4.4, and some experimental results are presented as examples. The effects of surface roughness and experimental nonlinearities are examined in Section 4.5.

#### 4.2 The Electron Mean Free Path

Extensive theoretical and experimental investigations of the electron mean free path have been performed; these have been reviewed by Powell [2]. Theoretical calculations [3] relate the electron escape depth  $L$  to the inelastic scattering mean free path, as mentioned in the Introduction. Experimentally [2],  $L$  is often determined by depositing a thin layer of material onto a substrate and monitoring the decreased Auger signal strength from the substrate atoms. The signal strength varies exponentially as  $e^{-x/L}$  with the thickness  $x$  of the layer, provided that the detector only accepts electrons which are emitted normal to the specimen surface. This exponential dependence is examined in the next section.

A compilation [4] of experimentally measured electron escape depths for several materials is shown in Fig. 3. Most of the data in this figure lies close to a universal electron escape depth curve which exhibits a minimum at an energy of  $\sim 100$  eV. Optimum depth resolution is obtained in an ASP experiment for electron kinetic energies at the escape depth minimum.

Several elastic and inelastic scattering mechanisms affect the Auger electron. Isotropic elastic scattering is usually ignored since as many electrons are scattered into a given direction as are scattered away from it [2]. In a crystalline solid where scattering is not isotropic, angular variations in the electron escape depth may become apparent [5].

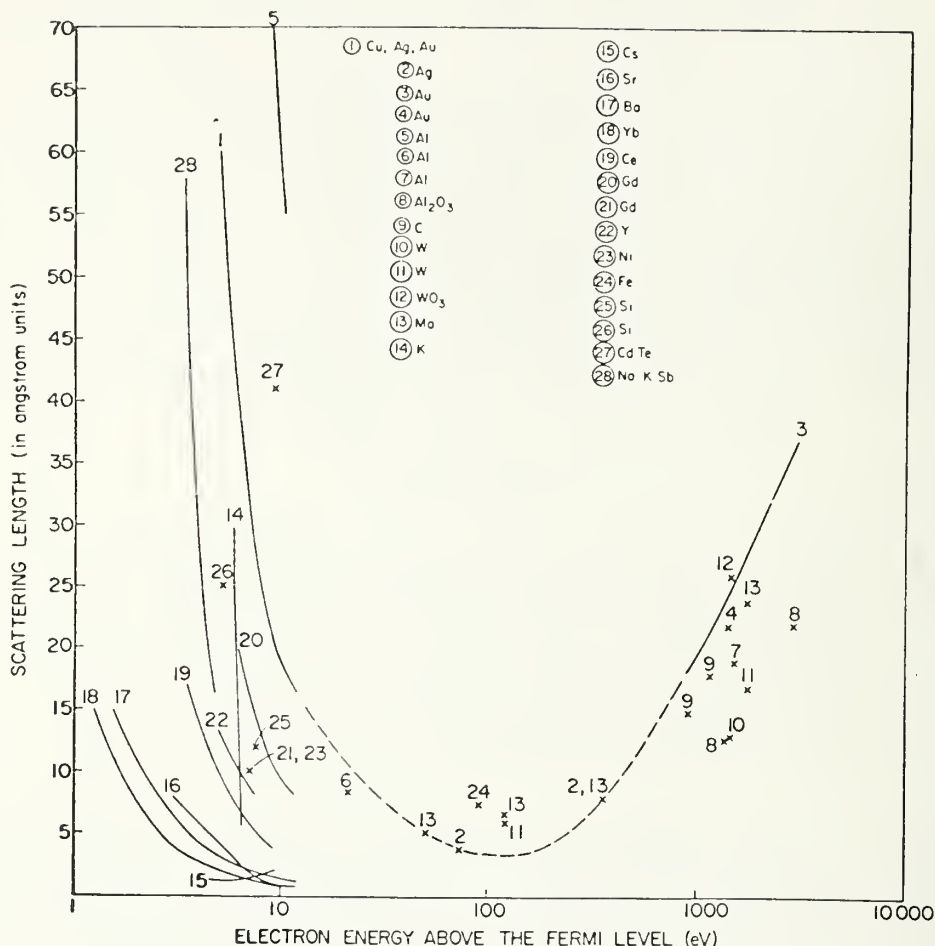


Fig. 3. Experimentally observed variations of the electron escape depth as a function of the electron energy. Compiled by Lindau and Spicer [4].

Electron-phonon scattering events are characterized by small energy losses [4], typically in the range of 10 to 50 meV, and are therefore negligible. The mean free path is thus independent of temperature. Electron-electron scattering mechanisms are of prime importance in determining the mean free path. Collective interactions such as bulk and surface plasmons and exchange and correlation effects need also be considered [6,7].

As the electron energy decreases below 100 eV, the escape depth increases. This is due, in part, to the fact that electrons lying well below the Fermi level in energy can no longer be excited into an unoccupied state. Beyond 100 eV, the escape depth increases as the collision cross section of the electron decreases.

#### 4.3 A Deconvolution Formula

The concentration of an element in an interfacial region may vary dramatically over distances of a few monolayers ( $\sim 1$  nm). An ASP depth profile of this interface will, of course, be broadened by the electron escape depth effect. In this section, we derive a simple deconvolution formula [8,9] which corrects for this broadening effect.

We mentioned in the last section that the Auger intensity varies exponentially with the depth of Auger emission. The exponential variation is based on the premise that a layer of thickness  $\Delta x$  has a probability  $(\Delta x/L)$  of scattering the Auger electron. The probability of an Auger electron traveling a distance  $x$  through  $x/\Delta x$  layers is then

$$\left(1 - \frac{\Delta x}{L}\right)^{x/\Delta x}. \quad (2)$$

If  $\Delta x \ll L$ , Eq. (2) reduces to  $e^{-x/L}$ . In most cases of practical interest, the exponential is a good approximation. However, in some cases of experimental interest,  $\Delta x$  may be the thickness of a monolayer and could then be a sizable fraction of  $L$ . In such a case, an approach similar to that leading to Eq. (2) is necessary. Gallon [10] describes such an approach.

We now define  $x$  to be a variable representing the position of the surface after some amount of sputtering in an ASP experiment,  $f(x)$ , the actual profile which we hope to determine, and  $A(x)$ , the measured Auger depth profile. We assume, for the moment, that the surface region is uniformly excited by the electron beam, i.e., the probability of creating an Auger electron does not vary with depth. This is generally a valid assumption since the high energy electrons used to stimulate Auger emission have larger mean free paths than the escape depth  $L$  of interest. Nonuniformity could be introduced by the backscattering effect, but we will defer consideration of this until Section 4.4. We also assume that the detected Auger electrons are emitted normal to the surface. We may express  $A(x)$  as a weighted sum of the actual concentration  $f(x)$  with the exponential probability of escape:

$$A(x) = \frac{1}{L} \int_0^{\infty} f(x + x') e^{-x'/L} dx'. \quad (3)$$

Note that, if  $f(x)$  is a flat profile,  $A(x) = f(x) \equiv f_0$ .

If Eq. (3) is integrated by parts, the desired deconvolution formula is immediately obtained:

$$f(x) = A(x) - L \frac{dA(x)}{dx}. \quad (4)$$

Thus, the actual concentration profile can be determined simply by differentiating the measured profile, multiplying by  $L$ , and subtracting the product from the measured profile.

It is most instructive to examine the derivation of Eq. (4) from first principles. Suppose then that a layer of material  $\Delta x$  is sputtered away. The change in signal flux  $\Delta A(x)$  has two components. The first component is the number of Auger electrons scattered by the layer  $\Delta x$ , which is proportional to the flux  $A(x)$  and the probability of scattering  $(\Delta x/L)$ . The second component is the number of Auger electrons produced in the layer of thickness  $\Delta x$ , which is proportional to  $f(x) \Delta x$ . We may write

$$\Delta A(x) = A(x) \left( \frac{\Delta x}{L} \right) - (\text{const}) f(x) \Delta x. \quad (5)$$

For a flat profile,  $A(x) = f(x) \equiv f_0$  and  $\Delta A(x) = 0$ ; thus, the constant must be  $1/L$ . We rewrite Eq. (4) as follows:

$$\frac{\Delta A(x)}{\Delta x} = \frac{A(x) - f(x)}{L}. \quad (6)$$

If we let  $\Delta x \rightarrow 0$ , Eq. (6) reduces to Eq. (4).

#### Example

Consider [11] a step function concentration profile (an abrupt interface) where

$$\begin{aligned}
 f(x) &= 0 & x < 0 \\
 f(x) &= 1 & x > 0 .
 \end{aligned}
 \tag{7}$$

Applying Eq. (3), we obtain

$$\begin{aligned}
 A(x) &= e^{x/L} & x < 0 \\
 A(x) &= 1 & x > 0 .
 \end{aligned}
 \tag{8}$$

$f(x)$  and  $A(x)$  are illustrated in Fig. 4. The measured profile is an exponential which has a width of  $2.2 L$  between the 10% and 90% points.

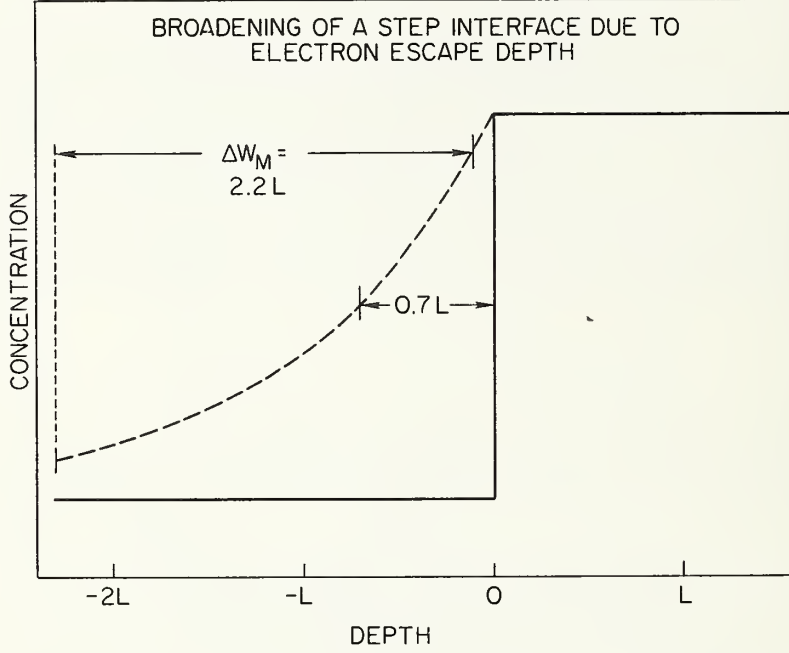


Fig. 4. Effect of escape depth broadening on a step function concentration profile. From Helms et al.[11].

#### 4.4 Off-Normal Detection

The previous derivation was restricted to normal detection of Auger electrons. If, instead, these electrons were emitted at an angle  $\theta$  to the surface normal, they would have to travel a distance  $x'/\cos \theta$  to emerge from depth  $x'$ . Equations (3) and (4) are corrected for this effect by replacing  $L$  with  $L \cos \theta$ :

$$A(x) = \frac{1}{L \cos \theta} \int_0^{\infty} f(x + x') e^{-x'/L \cos \theta} dx' \tag{9}$$

$$f(x) = A(x) - L \cos \theta \frac{dA(x)}{dx} . \tag{10}$$

As mentioned in Section 4.2,  $L$  may be a function [5] of  $\theta$ .

The actual Auger apparatus may accept electrons which are emitted at a variety of angles  $\theta$ . In this case, we write

$$A(x) = \frac{g(\theta) \int_0^\infty f(x + x') e^{-x'/L \cos \theta} dx' d\theta}{\int_0^\infty g(\theta) e^{-x'/L \cos \theta} dx' d\theta} . \quad (11)$$

Here,  $g(\theta)$  is the solid angle of acceptance for the detector. If we define

$$G(x') = \int f(\theta) e^{-x'/L \cos \theta} d\theta \quad (12)$$

we may rewrite Eq. (11) as follows:

$$A(x) = \frac{\int_0^\infty f(x + x') G(x') dx'}{\int_0^\infty G(x') dx'} . \quad (13)$$

Deconvolution may be performed numerically and is facilitated by approximating  $G(x')$  as follows:

$$G(x') \approx \sum_i G_i e^{-x'/L \cos \theta_i} \quad (14)$$

A useful approximation in some cases is to select an appropriate average value of  $\theta$  for use in Eq. (10).

One common electron detector used in Auger experiments is the cylindrical mirror analyzer (CMA). The CMA accepts electrons which are emitted at an angle of  $42.3 \pm 6$  deg about the CMA axis. If the specimen surface is normal to the CMA axis, an appropriate  $\theta_{\text{ave}}$  in Eq. (10) is 42.3 deg ( $\cos \theta_{\text{ave}} = 0.74$ ). The experiments described below were performed in a Varian 2730 Auger spectrometer in which the specimen normal is 30 deg off the CMA axis. We have numerically evaluated the response of this system to a step function concentration profile. The resulting profile has a 10% to 90% width of 1.65 L rather than 2.2 L. We choose  $\theta_{\text{ave}}$  such that  $2.2 (L \cos \theta_{\text{ave}}) = 1.65 L$  or  $\cos \theta_{\text{ave}} = 0.75$ .

Some examples relating to the measurement of the interface between silicon and silicon dioxide will clarify the deconvolution technique. First, however, we need to find appropriate values for the escape depth  $L$  in Si and  $\text{SiO}_2$ . Experimental measurements from two groups [4,12] are shown in Fig. 5 [13].

### Examples

We consider first an MNOS structure in which a layer of  $\text{SiO}_2$  is sandwiched between  $\text{Si}_3\text{N}_4$  and Si. An ASP experiment [14] is performed in which the  $O_{\text{KLL}}$  peak at 502 eV is monitored. The results are shown in Fig. 6. The dashed curve [8] is a numerical deconvolution accounting for the CMA geometry with  $L$  (502 eV) = 1.0 nm from Fig. 5. The points in the figure represent an application of Eq. (10) with  $\cos \theta_{\text{ave}} = 0.75$ . In both cases, the peak concentration of oxygen is increased by ~30%.

Next, we consider the Si- $\text{SiO}_2$  interface formed by thermal oxidation. The  $O_{\text{KLL}}$  (502 eV) and free  $\text{Si}_{\text{LVV}}$  (92 eV) peaks are monitored while sputtering through the interfacial region. (When Si is bonded to O, the LVV peak shifts from 92 to 78 eV.) A typical concentration profile [11] is shown in Fig. 7. This same profile is rescaled and drawn in Fig. 8. The dashed curves are the deconvolved profiles and were obtained through the use of Eq. (10) with  $\cos \theta_{\text{ave}} = 0.75$  as before. The oxygen profile is shifted to the right by ~0.8 nm and its 10% to 90% width changes from 3.8 to 3.3 nm. The silicon profile is shifted ~0.4 nm, and its 10% to 90% width is reduced from 2.2 to 2.1 nm. The distance between the 50% points of the oxygen and silicon profiles is reduced from 1.2 to 0.7 nm. This 0.7 nm difference is accounted for by the presence of an  $\text{SiO}_x$  phase in the interfacial region [15].



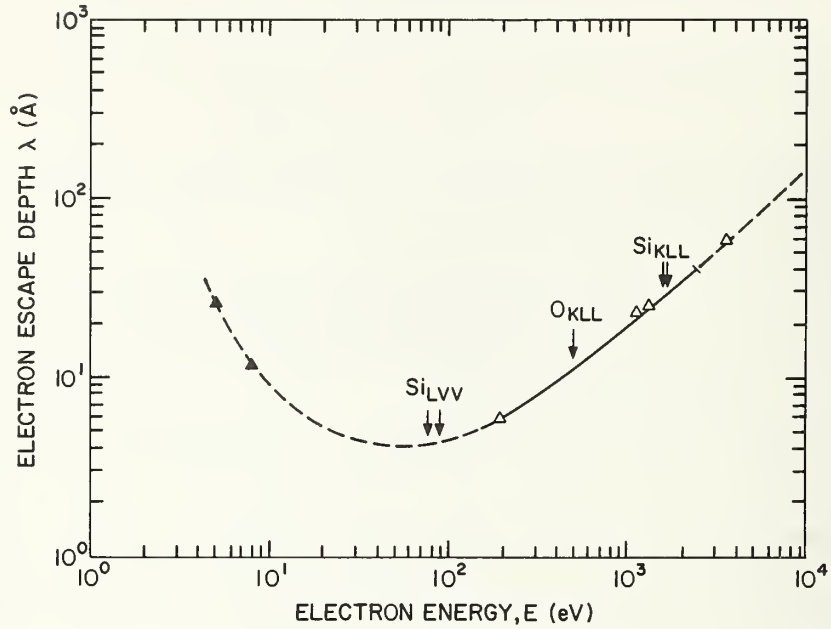


Fig. 5. Electron escape depths for Si and SiO<sub>2</sub> as a function of electron energy. Data of Lindau and Spicer [4] (▲) and Flitsch and Raider [12] (Δ) are shown.

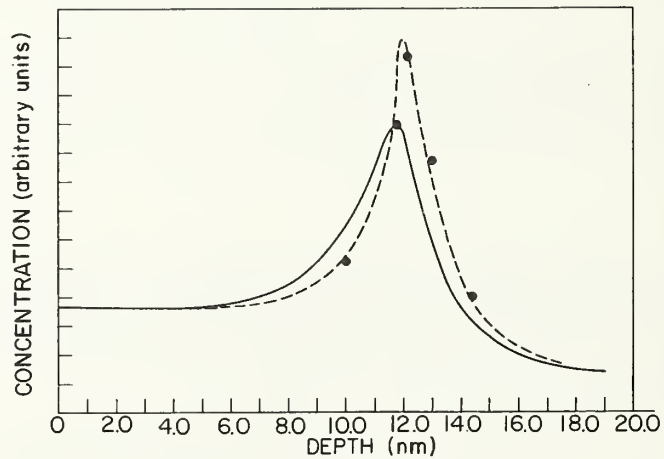


Fig. 6. Auger depth profile of the oxygen concentration in an MNOS sample (solid line). Numerical escape depth deconvolution (dashed line) and application of Eq. (10) (points) are shown. From Schwarz et al.[8].



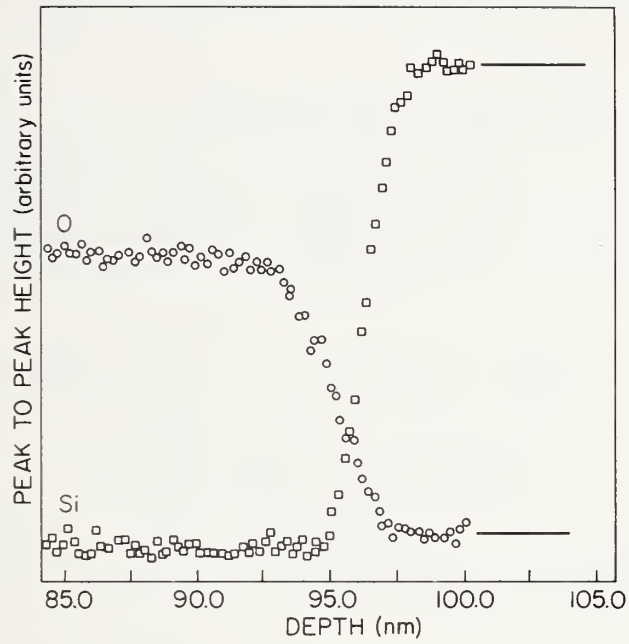


Fig. 7. Auger sputter profile of thermally grown Si-SiO<sub>2</sub> interface. From Helms et al. [11].

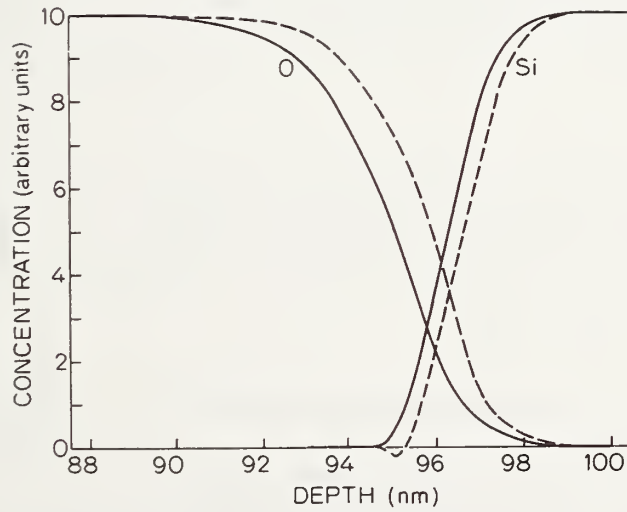


Fig. 8. An Auger sputter profile of the Si-SiO<sub>2</sub> interface (solid lines) is deconvolved through the use of Eq. (10) in the text (dashed lines).

It is interesting to note that, if the value for  $L$  (502 eV) used in Eq. (10) is too large, the deconvolved oxygen profile will initially rise above the bulk level before dropping to zero. Thus, the deconvolution technique provides an estimate of the upper limit of the value of  $L$ .

#### 4.5 Surface Roughness and Experimental Nonlinearities

Surface roughness has an obvious broadening effect on the Auger depth profile. In some cases, surface roughness may be induced by the ion beam [16]. In this section, we examine the electron escape depth broadening of a "linear" interface. The solution to this problem will indicate how surface or interface roughness and sputtering nonuniformities affect the measured profile. We will also investigate the effect of electron backscattering on the deconvolution technique.

Consider a specimen in which the concentration of an element is constant for some distance and then decreases linearly to zero over a distance  $\Delta x$ . This situation is illustrated in Fig. 9a. The measured profile is characterized by its width  $\Delta y_1$  and its position  $\Delta y_2$ . Here, we define  $\Delta y_1$  as the 10% to 90% width and  $\Delta y_2$  as the distance of the measured 50% point from the actual 50% concentration position in the specimen. A straightforward calculation using Eq. (3) leads to the results shown in Fig. 10. When  $\Delta x < L$ ,  $\Delta y_1 \sim 2.2 L$ , as noted previously. The  $\Delta y_2$  curve illustrates that the measured profile is shifted toward the specimen surface by a distance of  $\sim L$  in all cases. This effect was observed in the previous example.

These results apply to all of the situations illustrated in Fig. 9. For example, suppose the electron beam is not positioned in the center of the sputtered crater, but is instead located on a sloping portion of the crater edge. The Auger electrons will exit through a surface which is not parallel to the interface. Assume the interface is abrupt as in Fig. 9b. Over the width of the electron beam, the distance of the surface from the interface varies by an amount  $\Delta x$ . The results of Fig. 10 apply. Surface and interface roughness of order  $\Delta x$  are shown in Figs. 9c and 9d. Note that this roughness is symmetrical.

#### Examples

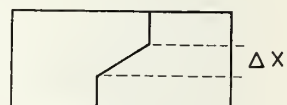
In the crater-edge profiling technique [1], a 5.0 nm depth profile is typically obtained by sweeping the electron beam over a lateral distance of 2 mm. The diameter of the electron beam may be 100  $\mu\text{m}$ . Thus, we have

$$\frac{5 \text{ nm}}{2 \text{ mm}} = \frac{\Delta x}{100 \mu\text{m}}$$

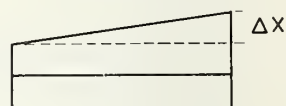
$\Delta x = 0.25 \text{ nm}$ ,  $\Delta x/L \sim 0.5$ , and from Fig. 10 we see that very little broadening is induced.

Next, we again consider the Si-SiO<sub>2</sub> interface profile of Fig. 8. We saw there that the measured oxygen profile had a 10% to 90% width of 3.8 nm. After deconvolution, this width was reduced to 3.3 nm and the curve was shifted 0.8 nm. As an approximation, we may use Fig. 10 with  $L = (0.75) 1.0 \text{ nm} = 0.75 \text{ nm}$ .  $\Delta y_1/L = 3.8/0.75 \cong 5.1$ . This corresponds to  $\Delta x/L \cong 6.0$  or  $\Delta x = 4.5 \text{ nm}$ . The original 10% to 90% width is  $(0.8) 4.5 \text{ nm} = 3.6 \text{ nm}$ . The shift corresponding to this  $\Delta x$  is  $\Delta y_2/L \cong 0.8$  or  $\Delta y_2 = 0.6 \text{ nm}$ .

Finally, we consider the effect of backscattering on the deconvolution technique. A certain fraction of the electron beam is backscattered by nuclei in the specimen and



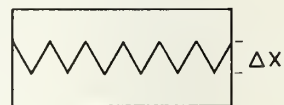
a. A linear interface



b. A sloping surface



c. Surface roughness



d. Interface roughness

Fig. 9. Four situations yielding equivalent measured profiles.

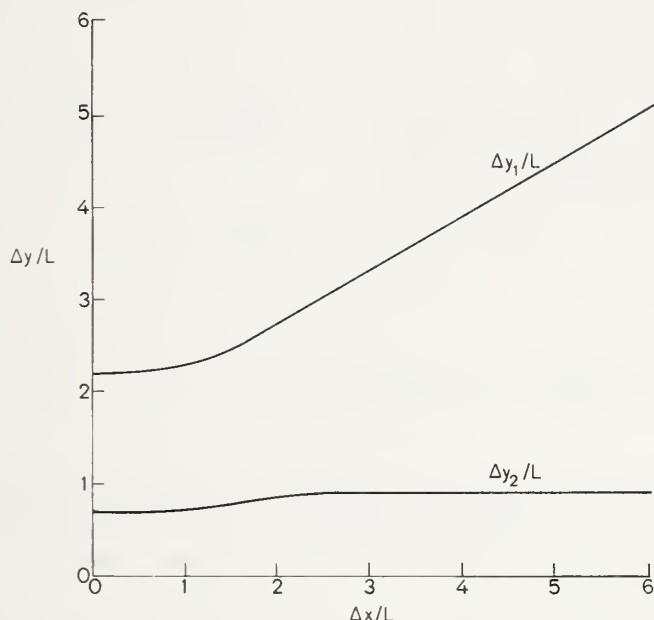


Fig. 10. The 10% to 90% width  $\Delta y_1$  and 50% position shift  $\Delta y_2$  as a function of the roughness parameter  $\Delta x$ .

redirected toward the surface where further Auger excitation can occur. In a homogeneous medium, backscattering does not affect the assumption of uniform excitation in the surface region. Backscattering coefficients differ from material to material. Smith and Gallon [17] show that the fraction of backscattered electrons increases with the electron energy and the mass of the nuclei. Thus, as one approaches an interface between two dissimilar materials, the backscattered component of the Auger signal will change, thereby affecting the measured profile. One can account for this by inserting an excitation function  $B(E, x)$  into Eq. (3):

$$A(x) = \frac{1}{L} \int_0^{\infty} f(x + x') B(E, x) e^{-x'/L \cos \theta} dx' . \quad (15)$$

It is also possible to account for electron beam attenuation or ion stimulated Auger in the excitation function. In this case,  $B$  is also a function of  $x'$ . Numerical deconvolution is again called for.

## 5. ION BOMBARDMENT EFFECTS

### 5.1 Introduction

In the previous chapter, we discussed a broadening mechanism inherent in the Auger detection process--the electron escape depth. We now turn our attention to a broadening mechanism inherent in the sputtering process--ion knock-on mixing.

Ions incident on a specimen surface create an atomic collision cascade in the bulk of the material. Some atoms in this cascade reach the surface and escape. The other atoms are displaced from their original position, resulting in a broadening of the measured depth profile. This process is illustrated in Fig. 11.

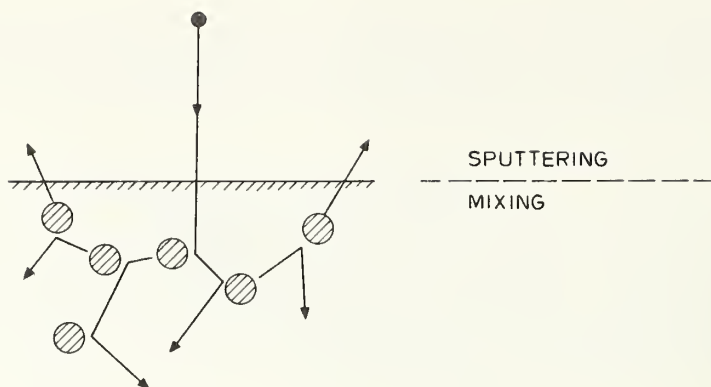


Fig. 11. Schematic illustration of the sputtering and mixing processes resulting from ion bombardment.

In this chapter, we will present elementary models of the sputtering [18] and mixing [19] processes. These models lead to simple formulas, allowing us to estimate the extent of sputtering and broadening as a function of the ion type, energy, and angle for a particular target material. We begin by developing a standard billiard-ball picture of atomic interactions in Section 5.2. The approach here is intuitive rather than rigorous so as to lend understanding to the models. In Section 5.3, the sputtering model is presented and compared to previous experimental and theoretical work. In Section 5.4, the ion knock-on mixing model is developed and compared to recent experimental data from ASP experiments and to other experiments and theory in the literature.

## 5.2 Atomic Interactions

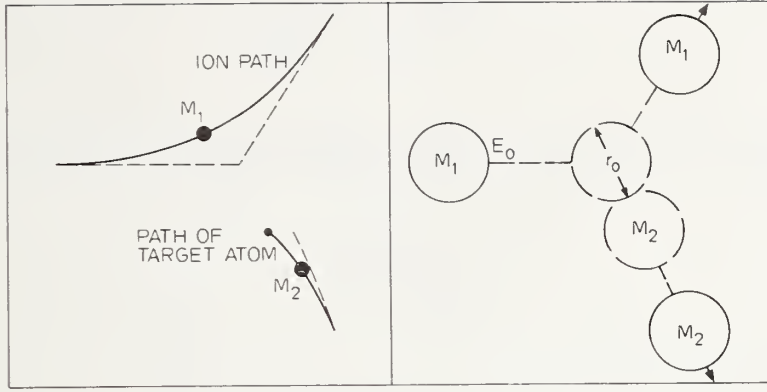
### 5.2.1 Introduction

A bombarding ion imparts most of its energy to nuclei and electrons in the specimen. Subsequently, this energy is transferred to phonons, raising the specimen temperature, and to other forms of radiation: x-rays, Auger electrons, etc. In Section 5.2.2, we examine the nuclear energy loss which is of prime importance in determining the movements of atoms and the resulting lattice damage. We present a standard billiard-ball model [20,21] of nuclear collisions which is commonly used to predict the range of the incident ion, i.e., the total path length travelled by the ion. In Section 5.2.3, we briefly examine the Firsov model [21,22] of electronic energy loss. We then conclude with a discussion of the Kinchin-Pease formula [23,24] which predicts the number of atomic displacements caused by the ion.

### 5.2.2 Nuclear Energy Loss

The nuclear energy loss process has been extensively studied in the last 50 years. Many models of varying sophistication have been developed; they have been reviewed by Carter and Colligon [20]. In the last decade, these models have been put to very practical use in the development of ion implantation [21].

Figure 12a is a schematic illustration of a nuclear collision in which a particle of mass  $M_1$  approaches and deflects an initially stationary particle  $M_2$ . These particles exert a mutual coulombic force on each other at all times. This force is, of course, greatest when the particles are closest together. At distances greater than 0.1 nm, the nuclei are effectively screened by their surrounding electrons, and the mutual force drops off quite rapidly with distance. The effective time of interaction then is actually quite short. Hence, nuclear collisions may be effectively modeled by instantaneous two-body collisions governed by conservation of momentum and energy. This classical billiard-ball model breaks down at very low energies [20] ( $\sim 10$  eV), where many-body collisions occur and at high energies [20,25] ( $> 1$  MeV), where quantum mechanical diffraction effects arise.



(a)

(b)

Fig. 12. (a) A particle of mass  $M_1$  approaches and deflects an initially stationary particle  $M_2$ . (b) These particles are modeled as billiard balls with adjustable radii. From Carter and Colligon [20].

The energy transfer and angular deflection in the collision illustrated in Fig. 12a are functions of the energy of particle 1. At low energies, the particle moves slowly, the interaction time is relatively long, and the transferred impulse (force-time product) is large. Thus, large angle scattering is expected. At high energies, the transferred impulse is smaller and the scattering angle decreases. This energy dependence is accounted for by allowing the radii of the hard sphere analogs in Fig. 12b to vary with energy. Specifically, the diameter of the sphere is defined as the distance of closest approach in a head-on collision between the two particles. The diameter is, therefore, dependent on energy and on the strength of the interatomic potential.

The distance of closest approach in a head-on collision is calculated as follows. Suppose particle 1 with mass  $M_1$  and energy  $E_0$  approaches a stationary particle of mass  $M_2$ . In the center-of-mass system (CM), the particles approach each other so that the net momentum is zero and the net energy [20] is

$$E_{CM} = \frac{M_2}{M_1 + M_2} E_0 \quad (16)$$

At the distance of closest approach,  $r_0$ , the kinetic energy in the CM system is completely converted to potential energy, i.e., the velocity of both particles drops to zero. Thus, we may write

$$V(r_0) = E_{CM} \quad (17)$$

where  $V(r)$  is the interatomic potential.

$V(r)$  may be expressed as a screened coulomb potential [20,21] as follows:

$$V(r) = f\left(\frac{r}{a}\right) \cdot \frac{Z_1 Z_2 e^2}{4\pi\epsilon_0 r} \quad (18)$$

where  $Z_1$  and  $Z_2$  are the atomic numbers of the two nuclei,  $e$  is the unit charge,  $f(r/a)$  is a screening function, and  $a$  is a screening length. For a single atom, the Thomas-Fermi screening length [26] is  $0.885 a_0 / Z^{1/3}$  where  $a_0$  is the Bohr radius (0.0529 nm). For two interacting atoms, the Thomas-Fermi screening parameter is an rms sum [20,21]:



$$a = 0.885 \frac{a_0}{\sqrt{Z_1^{2/3} + Z_2^{2/3}}} . \quad (19)$$

Many screening functions  $f(r/a)$  are found in the literature [20]. One of these,  $f(r/a) = a/r$ , is commonly used as it leads to a simple formula for the ion range. If this is substituted into Eq. (18), an inverse square potential is obtained:

$$V(r) \propto \frac{Z_1 Z_2}{r^2 \sqrt{Z_1^{2/3} + Z_2^{2/3}}} = \frac{c_1}{r^2} . \quad (20)$$

From Eqs. (17) and (20), we obtain

$$\frac{c_1}{r_0^2} = \frac{M_2}{M_1 + M_2} E_0 . \quad (21)$$

A most important quantity, both in this development and in the ion knock-on mixing model, is the mean free path between collisions  $\ell$ . According to the kinetic theory of gases [27],  $\ell$  is equal to the reciprocal of the product of the density of particles  $n$  and their interaction cross section  $\pi r_0^2$ . From Eq. (21), we have

$$\ell = \frac{1}{n\pi r_0^2} = \frac{1}{n\pi c_1} \frac{M_2}{M_1 + M_2} E_0 . \quad (22)$$

The probability of a collision after a particle has traveled a distance  $\Delta x$  is  $\Delta x/\ell$  (as in the electron escape depth case of Chapter 4).

The maximum kinetic energy which can be transferred from a particle of mass  $M_1$  and energy  $E_0$  to a stationary particle of mass  $M_2$  is  $\gamma E_0$ , where

$$\gamma = \frac{4M_1 M_2}{(M_1 + M_2)^2} . \quad (23)$$

For random scattering (isotropic scattering in the CM system), the average energy transfer in a collision [20] is  $(1/2) \gamma E_0$ .

In order to determine the ion range, we need to examine one further quantity, the stopping power  $(dE/dx)_{\text{nuc1}}$ , i.e., the energy loss per unit distance. This is usually calculated [20,21] by integrating a probable energy transfer over the scattering cross section  $\sigma$  as follows

$$\left( \frac{dE}{dx} \right)_{\text{nuc1}} = n \int T(\sigma) d\sigma . \quad (24)$$

We will make a quick estimate for  $(dE/dx)_{\text{nuc1}}$ , however, which leads to the proper result for the inverse square potential. We estimate the probable energy loss  $\Delta E$  in a length  $\Delta x$  by the average energy loss per collision  $(1/2) \gamma E_0$  multiplied by the probability of colliding  $\Delta x/\ell$ . This yields, with the use of Eq. (22),

$$\left( \frac{dE}{dx} \right)_{\text{nuc1}} = \frac{\gamma E}{2\ell} = \frac{n\pi c_1 \gamma (M_1 + M_2)}{2M_2} . \quad (25)$$

Equation (24) yields the same result. Note that, since  $\ell \propto E_0$ ,  $(dE/dx)_{\text{nuc1}}$  is independent of energy. This allows us to determine the ion range  $R$  as follows:



$$R = \frac{E_0}{\left(\frac{dE}{dx}\right)_{\text{nuc1}}} = \frac{2M_2 E_0}{n\pi c_1 \gamma (M_1 + M_2)} = 2kE_0 \quad (26)$$

where

$$k = \frac{0.0018}{n} \frac{\sqrt{Z_1^{2/3} + Z_2^{2/3}}}{Z_1 Z_2} \left( \frac{M_1 + M_2}{M_1} \right) \text{ nm eV}^{-1}. \quad (27)$$

As expected, the range decreases when the atomic sizes  $Z$  or density  $n$  increases. The parameter  $k$  plays an important role in the following sections.

Finally, it is necessary to consider the limitations of our choice of screening function  $f(r/a) = a/r$ . When  $r < a$  at high energies,  $f(r/a) > 1$  which is, of course, impossible. For  $r < a$ , then it is useful to let  $f(r/a) = 1$  and assume coulombic scattering. The form  $f(r/a) = a/r$  is also inaccurate for large  $r$ , i.e., at low energies. This is because, for  $E \gtrsim 100$  eV, the mean free path  $\ell$  predicted by Eq. (22) is less than the nearest neighbor distance  $d$  in the material. Below this energy, then, it is reasonable to let  $\ell$  remain constant and equal to  $d$ .

In Fig. 13,  $(dE/dx)_{\text{nuc1}}$  is plotted in terms of normalized parameters as a function of energy [20,28]. The constant  $(dE/dx)_{\text{nuc1}}$  of Eq. (25) is shown as a horizontal dashed line labeled  $S_v^{(0)}$ . The dash-dot line labeled  $S_e$  represents the electronic stopping power  $(dE/dx)_{\text{el}}$  which will be discussed in the next subsection. The solid curve is calculated numerically using a Thomas-Fermi screening function. The behavior of this curve can be illustrated by making estimates of  $(dE/dx)_{\text{nuc1}}$  at low and high energies as we did in Eq. (25), i.e.,  $(dE/dx)_{\text{nuc1}} \approx \gamma E_0 / 2\ell$ . At low energies, we let  $\ell = d$  and thus  $(dE/dx)_{\text{nuc1}} \propto E_0$ . At high energies,  $V(r_0) = c_2/r_0 = E_{\text{CM}}$  leads, from Eq. (22), to  $\ell \propto E_0^2$  and then, from Eq. (25),  $(dE/dx)_{\text{nuc1}} \propto 1/E$ . The  $E^{+1}$  dependence at low energies and  $E^{-1}$  dependence at high energies indeed describes the behavior observed in Fig. 13. We emphasize, though, that these estimates do not yield identical results to Eq. (24).

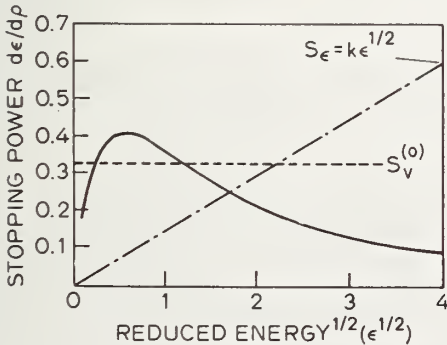
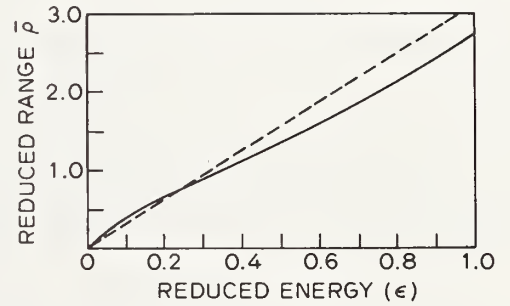


Fig. 13. Reduced stopping power as a function of reduced energy for the Thomas-Fermi potential (solid line), the inverse square potential (dashed line), and for electronic energy loss (dash-dot line). Parameters are defined in the text. (Viz. Refs. 20 and 28).

Fig. 14. Reduced range versus reduced energy for the Thomas-Fermi potential (solid line) and the inverse square potential (dashed line). Parameters are defined in the text. (Viz. Refs. 20, 28, and 29.)

In Fig. 14, the simple range equation, Eq. (26), is compared to the Thomas-Fermi range calculation [20,28,29]. We see that Eq. (26) is a good first approximation to the Thomas-Fermi theory. At low energies, Eq. (26) overestimates the range somewhat while, at high energies, it significantly underestimates the range.

The reduced parameters in Figs. 13 and 14 are defined as follows:

$$\epsilon = E_0 \cdot \frac{aM_2}{Z_1 Z_2 e^2 (M_1 + M_2)} \quad (28)$$

$$\rho = R \cdot \pi n \gamma a^2. \quad (29)$$

When  $\epsilon > 5$  in Fig. 14, the inverse square approximation becomes inaccurate. For Si incident on Si, this occurs at an energy of  $\sim 50$  keV. For Au incident on Au, this energy is  $\sim 1$  MeV.

### 5.2.3 Electronic Energy Loss

The theory of electronic energy loss is complex and need not be discussed here in detail. Lindhard and Winther [30] have shown that, over the energy range of interest here,  $(dE/dx)_{el}$  is proportional to the velocity of the ion:

$$\left(\frac{dE}{dx}\right)_{el} = k'E^{1/2}. \quad (30)$$

In the Firsov model [21,22] of electronic stopping, the constant  $k'$  is given by [21]

$$k' = 3.28(Z_1 + Z_2) M_1^{-1/2} n \text{ nm}^{-1} \text{ eV}^{1/2}. \quad (31)$$

The electronic energy loss is illustrated in Fig. 13 by the dash-dot line. At high energies, this is seen to be the dominant energy loss mechanism and therefore must be taken into account in a range calculation. This is done as follows:

$$R = \int_0^R dx = \int_0^{E_0} \frac{dE}{\left(\frac{dE}{dx}\right)_{nuc1} + \left(\frac{dE}{dx}\right)_{el}}. \quad (32)$$

From Eqs. (25) and (27),  $(dE/dx)_{nuc1} = 1/2k$  so that

$$R = \int_0^{E_0} \frac{dE}{\frac{1}{2k} + k'E^{1/2}} = \frac{2E_0^{1/2}}{k'} - \frac{1}{kk'^2} \ln \left(1 + 2kk'E_0^{1/2}\right). \quad (33)$$

Using the approximation  $\ln(1+x) \cong x - x^2/2 + x^3/3 \dots$ , we get

$$R \cong 2kE_0 \left(1 - \frac{4}{3} kk'E_0^{1/2}\right). \quad (34)$$

Since  $(dE/dx)_{nuc1}$  is independent of energy, we know that the total energy lost in nuclear collisions  $E_N$  is given by  $R = 2kE_N$ . Thus, we may rewrite Eq. (34) as follows:

$$\frac{E_N}{E_0} = 1 - \frac{4}{3} kk'E_0^{1/2}. \quad (35)$$

If  $E_N/E_0 < 1/2$ , it is best to use Eq. (33). These approximations will prove most useful in the sputtering model.

#### 5.2.4 Atomic Displacements

The number of atomic displacements  $N$  induced by the incident ion is predicted by the Kinchin-Pease formula [23,24] as follows:

$$N = \frac{E_N}{2E_d} \quad (36)$$

where  $E_N$  is the nuclear energy loss of the ion and  $E_d$  is the energy required to displace an atom from its lattice position. The assumption here is that, after  $N$  displacements have occurred, there are  $E_N/2E_d$  atoms traveling through the lattice with average energy  $2E_d$ . No further displacements can then occur, since one of the collision partners would have an energy less than  $E_d$ .

The choice of an appropriate  $E_d$  is somewhat controversial [20]. We have chosen an approach similar to Seitz [31] where we set

$$E_d = 4\Delta H_a \quad (37)$$

Here,  $\Delta H_a$  is the heat of atomization per atom. For example,  $E_d$  is 15.2 eV for Si. This value is commonly used [24,32]. The factor of 4 comes from two considerations. First,  $\Delta H_a$  accounts for the energies of half of each broken bond since these bonds are shared by neighboring atoms; hence, a factor of 2. Secondly, the lattice does not have time to relax. The relaxation energy is assumed to account for a further factor of 2. The uncertainty in the factor of 4 is accounted for in the models discussed in the next section.

#### 5.2.5 Summary

We have shown that, in a useful first approximation, the range  $R$  and the mean free path  $\ell$  are proportional to the ion energy. The constant of proportionality contains a charge term derived from a screened coulomb potential and a mass term derived from momentum conservation. At very low energies,  $\ell$  is approximated by the nearest neighbor distance  $d$ .

We have also seen that the electronic energy loss becomes significant at higher energies. A corrected range value and the nuclear energy loss  $E_N$  can then be easily determined.

Finally, we have seen that the number of atomic displacements caused by the incident ion is proportional to the nuclear energy loss  $E_N$  and inversely proportional to the bonding energy  $4\Delta H_a$ . All of these observations will prove useful in the following sections.

### 5.3 A Geometrical Model of Sputtering

#### 5.3.1 Introduction

The field of sputtering has been thoroughly reviewed by several authors [20,33]. Many models of the sputtering process have been proposed and can, in general, be classed into two categories. First are the simple or empirical models which usually are valid over a limited range of ion energy and contain adjustable parameters. Second are the more sophisticated models, requiring computer calculations which may involve Monte Carlo techniques or sets of integro-differential equations.

We have developed an elementary model of sputtering based on geometrical considerations which leads to a simple sputtering yield equation. The equation is valid over a broad range of ion energies (roughly 0.1 to 100 keV) and also accounts for the yield variation with the incident angle of the ion. For applicable materials, the accuracy of the equation is on a par with any of the other existing models.

In this section, we present a complete discussion of the sputtering model. The model is developed in Section 5.3.2, and necessary computations are performed in Section 5.3.3. Experimental comparisons are presented in Section 5.3.4. In Section 5.3.5, we discuss the assumptions and limitations of the model.

### 5.3.2 Development

In the sputtering process [20,33], an energetic ion incident on the target surface creates an atomic collision cascade in the bulk of the material. Some atoms in this cascade will reach the surface and escape. The sputtering yield  $S$  is defined as the number of atoms ejected per incident ion.

In order to model the sputtering process, it is useful to examine the region in which the collisions occur. We define a statistical region in which the atomic displacements are probable. At low ion energies, where the ion gives up most of its energy near the point of impact, the shape of this region is spherical. This does not suggest that the actual damage cluster has a spherical shape; rather, it implies that the probability of displacing an atom depends only on the distance of that atom from the point of impact.

The intersection of the statistical region with the target surface defines an affected surface area. The major assumption of our model is that the sputtering yield is proportional to this area. This assumption is supported by the experimental observation [20,33] that, irrespective of the ion energy, most sputtered atoms have energies of  $\sim 10$  eV and are emitted from a depth of a nanometer or so. Monte Carlo calculations [32] bear this out also.

We now define two parameters,  $A$  and  $B$ , which will be discussed in detail later on.  $A$  is the fraction of atoms in the statistical region which are displaced.  $B$  is the fraction of displaced atoms at the surface that actually escape. Thus, we find the volume of the statistical region as follows:

$$VOL = \frac{E/2E_d}{nA}$$

where  $n$  is the density of the material and  $E/2E_d$ , from the Kinchin-Pease formula Eq. (36), is the number of displacements caused by the ion. (Henceforth,  $E$  refers specifically to the nuclear energy loss  $E_N$ .)

The sputtering yield  $S$  is given by

$$S = B(An)^{2/3} \cdot AREA. \quad (39)$$

Here,  $(An)^{2/3}$  is the number of displaced atoms per unit surface area, and the  $AREA$  is, of course, defined by the intersection of the statistical region with the surface.

We might expect the affected area to be related to the volume as follows:

$$AREA = f(E) \cdot (VOL)^{2/3}. \quad (40)$$

We would then have, from Eqs. (38) and (39),

$$S = B \left( \frac{E}{2E_d} \right)^{2/3} f(E). \quad (41)$$

In fact, we will obtain an equation of this form.

As a first example, suppose that the disturbed region is spherical with a radius  $r$  and centered at a depth  $\lambda$  below the surface ( $\lambda < r$ ). The area defined by the intersection of the sphere with the surface is easily shown to be



$$\text{AREA} = \pi r^2 \left(1 - \frac{\lambda^2}{r^2}\right). \quad (42)$$

From Eq. (38), we know that

$$\frac{4}{3} \pi r^3 = \frac{E/2E_d}{nA}. \quad (43)$$

If we assume  $\lambda \ll r$ , we readily find from Eq. (39) that

$$S = B\pi \left(\frac{3E}{8\pi E_d}\right)^{2/3}. \quad (44)$$

Thus, at very low energies, we might expect the yield to vary as  $E^{2/3}$  and inversely as the bonding energy  $E_d^{2/3}$ .

Note that, for  $\lambda = 0$ , the shape of the statistical region is hemispherical. Equation (43) for the full sphere is still used, however. Half the incident ion energy is assumed to be carried off by the sputtered atoms. We will elaborate on this argument later. It is also important to note that the surface atoms are acted upon from one side only, i.e., from the interior of the specimen. Thus, we might expect the value of  $B$  to be 0.5 if all displaced surface atoms escape and  $B \sim 1$  if contributions from deeper layers are included. In fact, we will show that  $B \sim 0.2$  in most materials. Finally, we observe that the parameter  $A$  does not appear in Eq. (44).

We know that the incident ion does not release its energy immediately upon impact; rather, the ion travels some distance into the target, releasing its energy gradually. Again, we will make use of a statistical quantity  $k$  representing the energy loss rate averaged over many incident ions. Recall that the total ion range is  $R = 2kE$ .

We expect the statistical region to be a perturbation of the sphere. The perturbed or elongated sphere is treated most naturally as an ellipsoid with major axis  $a$  and minor axis  $b$  as in Fig. 15. The volume of the ellipsoid is  $(4/3)\pi ab^2$  and from Eq. (38) we have

$$\frac{4}{3} \pi ab^2 = \frac{E/2E_d}{nA}. \quad (45)$$

The area defined by the intersection of the ellipsoid centered at depth  $\lambda$  with the surface is (for normal ion incidence)

$$\text{AREA} = \pi b^2 \left(1 - \frac{\lambda^2}{a^2}\right). \quad (46)$$

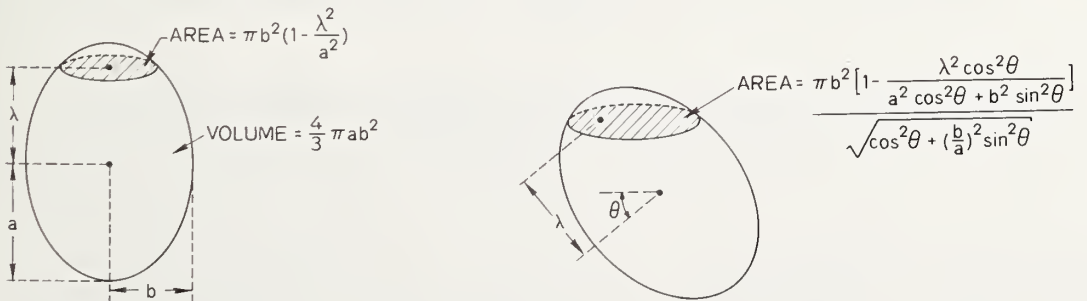


Fig. 15. Definition of ellipsoid parameters and cross-sectional areas.

The ellipsoid is centered about the path of the ion, which suggests that we let  $\lambda$  equal half the ion range:

$$\lambda = kE . \quad (47)$$

We now define the length of the ellipsoid as a perturbation of the sphere, so that

$$a = r + \lambda . \quad (48)$$

where  $r$  is defined in Eq. (44) and  $\lambda$  is half the range. We also assume that the damage volume is the same so that

$$ab^2 = r^3 . \quad (49)$$

At low energies, when  $\lambda \ll r$ ,  $a \sim r$  and the statistical region is a hemisphere as before. At high energies,  $a \sim \lambda$ , and the length of the ellipsoid is nearly equal to the ion range.\*

It is again important to recognize that the ellipsoid is a statistical construct which allows us to predict the degree to which the surface is excited. The actual path of the ion is not a straight line into the solid, and the damage cluster formed by the ion will not resemble an ellipsoid. The true path of the ion is irrelevant to the sputtering process, however, so long as it does not return to the surface. (This is unlikely at near normal incidence.) Thus, for computational purposes, we treat the ion as though it travels a straight line path.

Substituting Eqs. (48) and (49) into Eq. (46), we obtain

$$\text{AREA} = \pi \frac{r^3}{r + \lambda} \left( 1 - \frac{\lambda^2}{(r + \lambda)^2} \right) . \quad (50)$$

In this form, refinements to  $\lambda$  or  $r$  (i.e., to the range estimate or the Kinchin-Pease formula) can be incorporated.

Substituting for  $r$  and  $\lambda$  from Eqs. (44), (47), and (45), we obtain

$$S = B \left( \frac{3\pi}{8E_d} \right)^{2/3} \frac{E^{2/3}}{1 + \beta E^{2/3}} \left( 1 - \left( \frac{\beta E^{2/3}}{1 + \beta E^{2/3}} \right)^2 \right) \quad (51)$$

where

$$\beta = k \left( \frac{8}{3} \pi E_d A n \right)^{1/3} . \quad (52)$$

Note that this is in the form of Eq. (41).

If the ion is incident at an angle  $\theta$  to the surface normal, as in Fig. 15, the AREA of Eq. (46) becomes

$$\text{AREA} = \pi b^2 \left( 1 - \frac{\lambda^2 \cos^2 \theta}{a^2 \cos^2 \theta + b^2 \sin^2 \theta} \right) \left( \cos^2 \theta + \left( \frac{b}{a} \right)^2 \sin^2 \theta \right)^{-1/2} . \quad (53)$$

This leads to an equation similar to Eq. (51), which we present in the next subsection.

---

\* Another way to define the length of the ellipsoid is to set the distance between foci equal to the ion range. In this case,

$$a^2 - b^2 = \lambda^2 .$$

This assumption considerably complicates the resulting equations, but it could be used in a computer calculation.



### 5.3.3 Computation

We note in Eq. (51) that the parameter  $A$  appears only in the expression for  $\beta$ , and there it is raised to the  $1/3$  power. Thus, the equation is relatively insensitive to variations of  $A$ . We have found that, in all of our comparisons to this experiment, good results are obtained with  $A = 0.0012$  ( $A^{1/3} \sim 0.1$ ). We will discuss this parameter further in the next subsection. If we let  $A = 0.0012$ , we have

$$\beta = 0.343 k(n\Delta H_a)^{1/3} \text{ eV}^{-2/3} . \quad (54)$$

The definitions of  $k$ ,  $k'$ ,  $\Delta H_a$ , and  $E$  (the nuclear energy loss) are found in Section 5.2.

If we define

$$x = \frac{\beta E^{2/3}}{1 + \beta E^{2/3}} , \quad (55)$$

Eq. (51) can be rewritten as

$$S = 0.302 \frac{B}{\beta (\Delta H_a)^{2/3}} x(1 - x^2) . \quad (56)$$

In the case where  $\theta \neq 0$ , we let

$$x^2 = \frac{(\beta E^{2/3})^2 (1 + \beta E^{2/3})}{\sin^2 \theta + (1 + \beta E^{2/3})^3 \cos^2 \theta} . \quad (57)$$

Then,

$$S = 0.302 \frac{B}{\beta (\Delta H_a)^{2/3}} x(1 - x^2 \cos^2 \theta) . \quad (58)$$

When  $\theta = 0$ , Eqs. (57) and (58) reduce to Eqs. (55) and (56).

The maximum sputtering yield  $S$  occurs at an energy  $E_{\max}$  for which  $dS/dx = 0$ . From Eq. (58), this leads to

$$x_{\max} = \frac{1}{\sqrt{3 \cos \theta}} . \quad (59)$$

In particular, when  $\theta = 0$ , Eq. (59) leads to

$$E_{\max} = 1.60\beta^{-3/2} \text{ eV} . \quad (60)$$

The variation of the sputtering yield at normal incidence as a function of energy is illustrated pictorially in Fig. 16. The normalized yield  $S[B(3\pi^{1/2}/8E_d)]^{-1}$  is plotted in Fig. 17 as a function of the nuclear energy loss for several values of  $\beta$ .

### 5.3.4 Experimental Comparisons

We used Sigmund's [33] compilation of experimental data to test the sputtering model. Figure 18 illustrates the application of Eq. (56) to silver with  $B = 0.30$ . The figure shows experimental data points and the low and high energy theoretical curves of Sigmund [33] (dashed lines). The heavy solid lines are calculated from our model and agree well with the experiment. Comparisons were also made for Si, Ge, Cd, Zn, Pd, Cu, and Au from Sigmund's paper. In each case, good results were obtained with  $A = 0.0012$ . Values of the surface factor  $B$  which best fit the data are listed in Table 2.

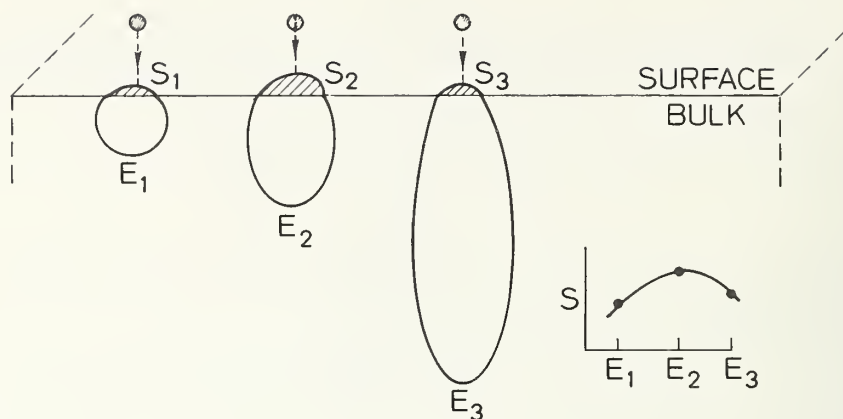


Fig. 16. Illustration of the sputtering yield variation with ion energy.

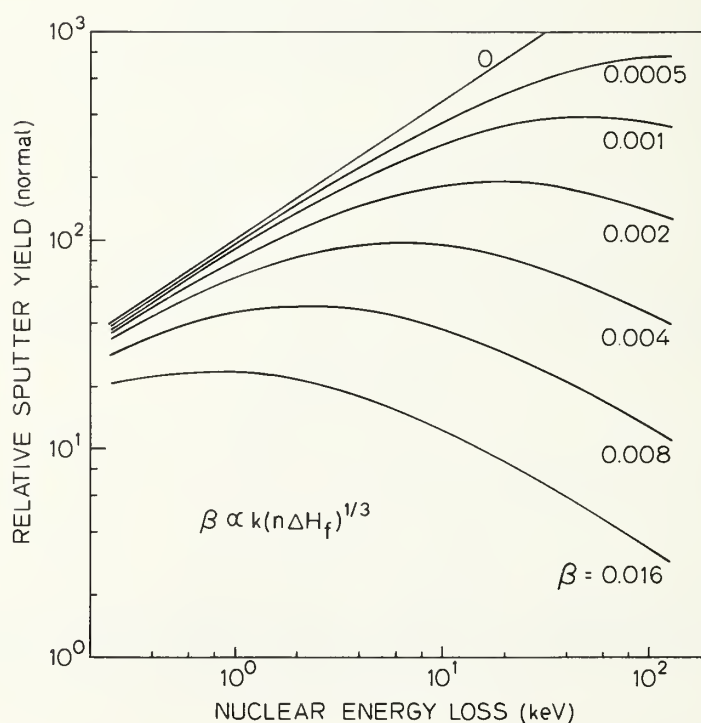


Fig. 17. The relative sputtering yield is plotted as a function of the nuclear energy loss  $E$  for several values of  $\beta$ .

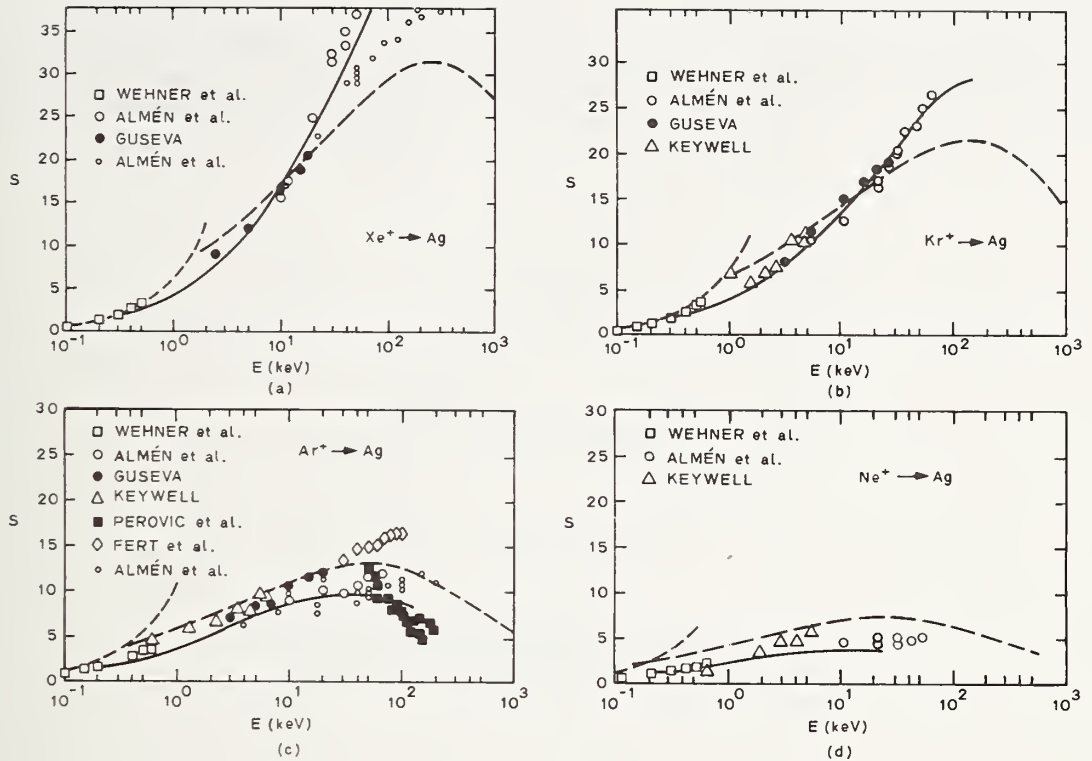


Fig. 18. Sputtering yields of Ag versus ion energy for (a)  $\text{Xe}^+$ , (b)  $\text{Kr}^+$ , (c)  $\text{Ar}^+$ , and (d)  $\text{Ne}^+$  ions at normal incidence. Data compilation from Sigmund [19]. Solid curves result from the present model. Sigmund's theoretical curves (dashed) are also shown.

Table 2

VALUES OF SURFACE  
FACTOR B

Element	B
Si	0.10
Ge	0.14
Cu	0.18
Zp	0.27
Pd	0.23
Ag	0.30
Cd	0.36
Au	0.45

Surface factors  
derived from Sigmund's  
data compilation [33].

The surface factor B can be determined from the work of Rosenberg and Wehner [34], who measured the sputtering yields of many elements under 400 eV  $\text{Xe}^+$  bombardment. Note that  $\beta$  for  $\text{Xe}^+$  is typically very small due to the short range, i.e., small value of k. Reference to Fig. 17 indicates that, at 400 eV, the relative sputtering yield is nearly independent of the substrate. For 400 eV  $\text{Xe}^+$ , Eq. (59) reduces to

$$S \propto \frac{B}{(\Delta H_a)^{2/3}}. \quad (61)$$

Thus, B is determined by multiplying the measured yield by  $(\Delta H_a)^{2/3}$ . It is interesting to note that previous low energy sputtering theories [33] contain a  $1/E_b$  dependence where  $E_b$  is a surface binding energy bearing a strong relation to  $\Delta H_a$ . The values of B, determined from Rosenberg and Wehner, are plotted in Fig. 19. These values are normalized to  $B = 0.30$  for silver. They agree fairly well with the values obtained in Table 2. Discrepancies may be due to various second-order effects, such as Xe saturation. Figure 19 illustrates two trends: a periodic dependence and a mass dependence. Note that Zn and Cd in Table 2 continue the upward trend observed in the transition metals. In Fig. 20, we have divided B by  $\sqrt{M}$  for the transition metals and plotted the results in relation to the periodic table. (In addition to the values derived from Wehner, Zn and Cd from Table 2 are included in the figure.) We will discuss these results further in the next subsection.

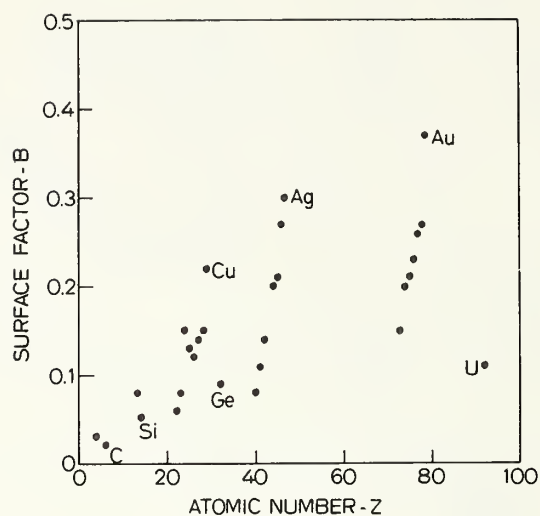
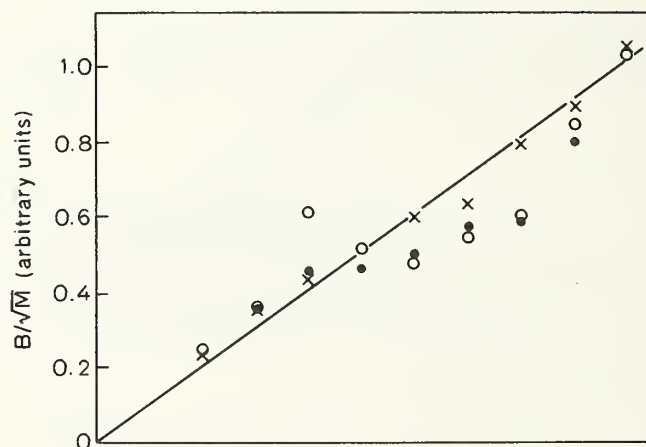


Fig. 19. The surface factor B derived from Rosenberg and Wehner [34] is plotted as a function of atomic number Z.



Sc	Ti	V	Cr	Mn	Fe	Co	Ni	Cu	Zn
	o	o	o	o	o	o	o	o	o
Y	Zr	Nb	Mo	Te	Ru	Rh	Pd	Ag	Cd
	x	x	x		x	x	x	x	x
La	Hf	Ta	W	Re	Os	Ir	Pt	Au	Hg
		•	•	•	•	•	•	•	

Fig. 20. The surface factor B is divided by the square root of the atomic mass and plotted in relation to the periodic table for the transition metals.

Support for the  $Z$ , or mass dependence, of the sputtering model comes from the experimental data of EerNisse [35], who measured the sputtering yield of Au for low fluence 45-keV ion bombardment. Figure 21 shows a comparison of his experimental data with the prediction of the present model. Reference to Eq. (28) indicates that the model still has validity for light ion ( $\text{He}^+$ ) bombardment of Au.

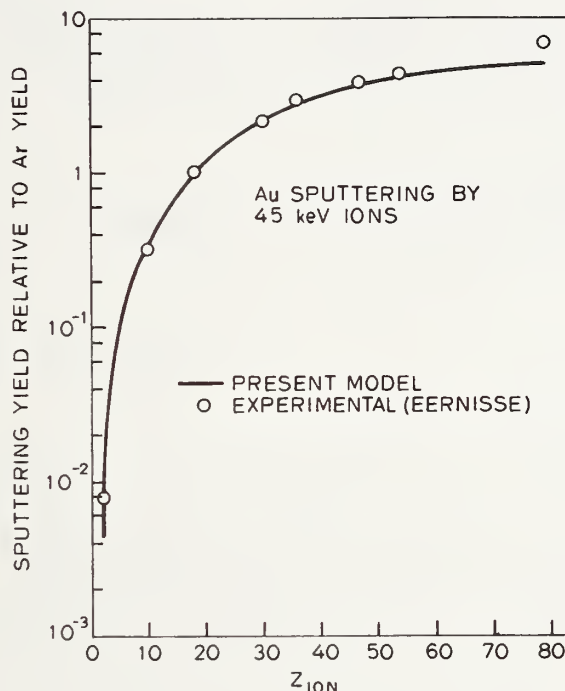


Fig. 21. Sputtering yields of Au bombarded by 45-keV ions normalized to  $\text{Ar}^+$  yield. Solid curve results from the present model. Points are from experimental data of EerNisse [35].

Next, we consider the angular dependence of the model. Figure 22 demonstrates pictorially that the angular dependence of the sputtering yield is a function of energy. Rol et al. [36] observed this effect in polycrystalline Cu. Their experimental results are compared with the sputtering model in Fig. 23. Molchanov et al. [37] observed the yield variation of polycrystalline Cu with the incident angle for 27-keV  $\text{Ar}^+$  ions. Their experimental data agrees well with the model, as shown in Fig. 24. At large angles, the ion may escape from the sample before depositing all of its energy. This probably accounts for the discrepancy between the model and experiment for  $\theta > 70^\circ$ . At 27-keV, the angular dependence is described very well by a  $1/\cos \theta$  variation. (The  $1/\cos \theta$  dependence is a common approximation [36].) Actually, this is a coincidence. At higher energies, the angular dependence curve will lie above the 27-keV curve. At low energies, the angular dependence curve will lie considerably below the 27-keV curve. As an example, for 2-keV  $\text{Ar}^+$  bombardment, according to the model, the sputtering yield of Cu never increases by more than 40%.

### 5.3.5 Discussion

We have seen that the sputtering model just described agrees well with much experimental data in the literature. It is important now to discuss the assumptions we have made and determine the limits of applicability of the model. At the outset, we note that the model does not account for any of the following effects:



- (1) channeling or focusing,
- (2) multicomponent systems,
- (3) ion beam flux dependence,
- (4) reactive sputtering, and
- (5) saturation with the sputtering species.

The model is strictly applicable to an amorphous material. Reasonable results may be obtained in crystalline materials if the ions are not incident along a channeling direction. Multicomponent systems can sometimes be treated in an approximate way. In the next section,  $\text{SiO}_2$  is modeled as a lattice of Ne atoms with reasonable success.

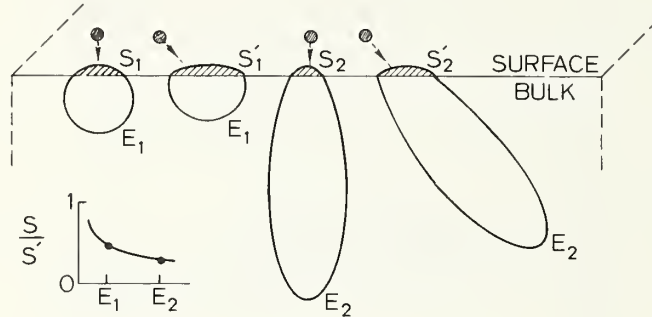


Fig. 22. Pictorial representation of the sputtering yields angular dependence. The normal-to-glancing incidence ratio of sputtering yields decreases with energy due to the increasing asymmetry of the disturbed volume.

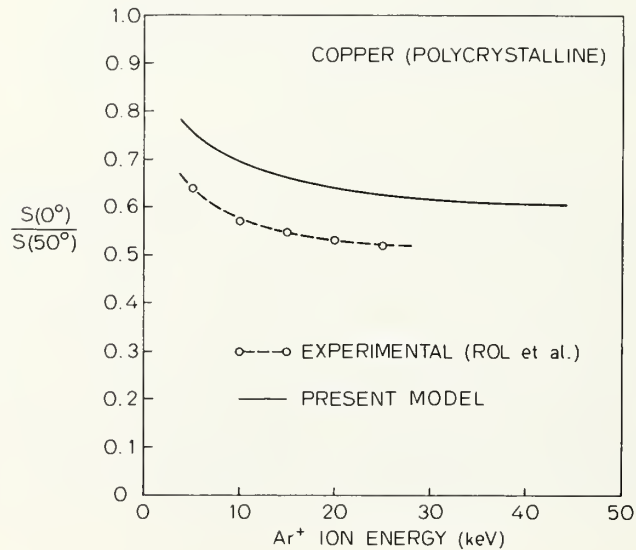


Fig. 23. Sputtering yield ratios at normal and  $50^\circ$  incidence versus  $\text{Ar}^+$  ion energy; experimental [36] and theoretical.

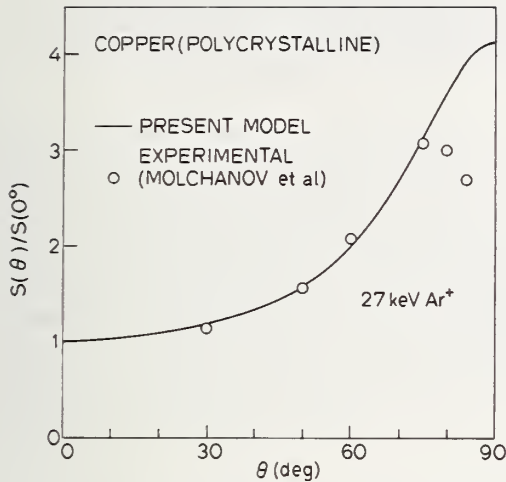


Fig. 24. Relative sputtering yield increases as a function of incident angle; experimental [37] and theoretical.

factor  $B$  which we defined as the fraction of excited surface atoms that actually escape.  $B$  is strictly a property of the sample surface and does not depend on the mass or energy of the impinging ion. The straight-line fit of Fig. 20 suggests the following empirical relation for this scale factor:

$$B = (\text{geometric factor})(\text{number valence electrons})\sqrt{M}. \quad (62)$$

The geometric factor is related to the number of exposed atoms and may account, in part, for the sputtering yield variation observed on different crystalline faces. For the close-packed transition metals of Fig. 20, this factor is relatively constant. Since we have already accounted for the lattice binding energy in the bulk calculation, the observed variation of  $B$  must be related to an additional surface energy barrier. In this section, we suggest one possible model for the scale factor  $B$  which is consistent with the empirical relation.

To begin, we must first examine the energy and charge state of sputtered atoms. Many workers have observed that the distribution of sputtered atoms peaks at an energy of only a few electron volts and falls off rapidly with increasing energy [20]. The Monte Carlo calculations of Harrison et al. [38] for Cu show this peak to occur at  $\sim 2$  eV with a  $1/E$  falloff thereafter, consistent with experimental results. The great majority of sputtered atoms are neutral (>99% in most cases) [39]. Prival [39] recently proposed a model of sputtered ion emission in which a sputtered atom is initially displaced as an ion core and then neutralized. He considers an atom with an average emission energy and determines its probability of neutralization using a free electron density of states in the metal. The results are consistent with observed neutral-to-ion yield ratios.

An ion must surmount an additional surface energy barrier due to the coulomb image force. The additional energy is on the order of the electron work function (less due to correlation and exchange) and should have a magnitude of a few electron volts. This energy is quite significant since the distribution of excited surface atoms is heavily weighted at low energies. A large majority of the atoms which are excited at the surface have an imparted energy of 10 eV or less. Those which are quickly neutralized have a much greater chance of escaping than those which remain ionized. As a first approximation, we suggest that  $B$ , the fraction of escaping atoms, varies monotonically with the neutralization probability of an emitted ion. The neutralization probability may be roughly proportional to the number of valence electrons which can interact with the ion, as desired. Alternatively, the neutralization probability could be related to the periodic behavior of the ionization potential [40]. The  $\sqrt{M}$  dependence may arise as follows. The energy

The parameter  $A$ , defined earlier as the fraction of atoms in the statistical region which are displaced, is assumed constant in all materials. Since the sputtering equations depend only on  $A^{1/3}$ , small variations in  $A$  will have little effect. The value of  $A = 0.0012$  may seem small, but two things must be remembered. First, the statistical region is probably larger than the actual damage cluster. Secondly, in Eq. (52) the product  $AE_d$  appears.  $E_d$  is defined as  $4\Delta H_a$ , but the assignment of the factor of 4 is debatable, as discussed in Section 5.2. The uncertainty in this factor is incorporated into the value of  $A$ .  $A$  should not vary strongly with ion energy since the energy lost per unit distance by the ion is a constant independent of energy in our approximation. At high energies where  $S_n(E)$  begins to decrease, this may no longer be true.

We have, to this point, modeled sputtering as a bulk process and predicted the extent to which the surface is excited. The absolute yield is obtained using a scale

distribution of emitted atoms is roughly the same in most materials due to an equipartitioning of the incident ion energy. Since the velocity  $v$  equals  $\sqrt{2E/M}$ , sputtered atoms from light materials have significantly greater velocities. The probability of neutralization is expected to be proportional to the time spent within some mean distance of the surface and hence to  $\sqrt{M}$ . Further comparisons to elemental sputtering data should prove useful in testing the validity of this model.

The first-order range approximation  $\lambda = kE$  allows us to develop a fairly simple sputtering equation. At low energies where  $\lambda \ll r$ , the accuracy of this approximation is unimportant. At higher energies, the constant stopping power approximation allowed us to continue using an ellipsoidal statistical region (rather than a pear-shaped distribution in which more displacements occur on one end than the other). At high energies, the approximations break down in several respects. The range is underestimated, and therefore the yield will probably be overestimated. The electronic energy loss and the nuclear energy loss vary as the ion travels deep into the solid. The values near the surface are important, however. If one uses a value of  $k$  such that  $1/2k = (dE/dx)_{\text{nuc1}}$  at  $E_0$ , better answers will be obtained at high energies.

### 5.3.6 Summary

In this section, we have developed a sputtering model which is easily implemented and predicts the yield dependence on ion mass and incident angle over a broad range of energies. The relative sputtering yield can be predicted without any adjustable parameters. A scale factor  $B$  is derived from experiment and yields information about the sample surface. An empirical relationship for  $B$  is suggested in the text and appears to work well.

Experimental comparisons indicate that the model is reasonably accurate. We emphasize that the model is not rigorous, but rather is based on a number of reasonable assumptions. Thus, the use of sophisticated calculations for the range or the number of displacements does not appear justified at this time. The sputtering model should prove to be of practical use to experimentalists and designers.

## 5.4 An Ion Knock-On Mixing Model

### 5.4.1 Introduction

Depth profiles obtained from ASP or SIMS experiments are broadened by ion beam-induced atomic mixing [32,16,42]. This effect was illustrated in Fig. 11. In Section 5.4.2, we develop a model for ion knock-on mixing [19] based on an analogy to thermal diffusion theory. The model leads to a simple relationship which predicts the broadening observed in a sputter profiling experiment. We show that the broadening of the Si-SiO<sub>2</sub> interface for low energy Ne<sup>+</sup>, Ar<sup>+</sup>, and Xe<sup>+</sup> bombardment is consistent with the mixing model in Section 5.4.3. We then extend the model to higher energies and compare it to Monte Carlo calculations [32] and experimental data in Section 5.4.4.

### 5.4.2 Development

The ion knock-on mixing model [19,41] developed here is based on an analogy to thermal diffusion theory. A similar approach has been taken by Haff and Switkowski [42]. In their paper, an effective diffusion coefficient  $D$  is derived in terms of various parameters, including a cascade radius and the stopping power of the ion. A diffusion time  $t$  must be inferred in order to determine the broadening observed in a sputter profiling experiment. In our model, an effective broadening parameter  $W^2 = Dt$  is derived and expressed in terms of the sputtering yield  $S$ , a measurable quantity. The stopping power effect in Haff's model is inherent in the sputtering yield.

Our derivation is based on the assumption that an atom in the bombarded solid undergoes a number of random collisions  $N$  and is detected immediately prior to or after its escape from the surface. In an ASP experiment, this assumption is valid if the escape

depth  $L$  is small ( $\sim 0.5$  nm) or is much less than the ion broadening parameter  $W$ . In a SIMS experiment, atoms are detected after their escape. We describe the path of the atom by a random walk as illustrated in Fig. 25. Monte Carlo calculations [32] confirm that the assumption of random collisions at low and moderate ion energies is reasonable. The net distance  $R$  traveled by the atom is given by

$$R^2 = N \overline{a^2} \quad (63)$$

where  $\overline{a^2}$  is the mean square step length.

In order to determine  $N$ , we again make use of the Kinchin-Pease formula, Eq. (36), which states that the number of atomic displacements occurring in the solid per incident ion is  $E/2E_d$ . The number of collisions which occur is twice the number of displacements since two atoms collide with each other in a displacement event. Suppose now that the specimen of interest has been sputtered for a time sufficient to reach equilibrium.  $N$ , the number of collisions suffered by an escaping atom, is simply the total number of collisions which have occurred, divided by the total number of escaping atoms. If we normalize to the number of incident ions, we obtain

$$N = \frac{\# \text{ collisions/ion}}{\# \text{ escaping atoms/ion}} = \frac{E/E_d}{S} \quad (64)$$

$S$ , of course, is the sputtering yield.

In diffusion theory, a broadening parameter  $Dt$  is defined as  $Dt = (1/6) N \overline{a^2}$ . We now define an analogous broadening parameter

$$W^2 = \frac{1}{6} N \overline{a^2} = \frac{E a^2}{6 E_d S} \quad (65)$$

For low ion energies ( $E_0 < 1$  keV), most collisions occur at energies of several  $E_d$ .  $a$  should then be roughly the nearest neighbor distance  $d$  in the solid (0.3 nm). At higher energies,  $\overline{a^2}$  is given by

$$\overline{a^2} = \frac{\int \ell^2(\epsilon) N(\epsilon) d\epsilon}{\int N(\epsilon) d\epsilon} \quad (66)$$

where  $N(\epsilon) d\epsilon$  is the number of collisions occurring in the interval  $d\epsilon$  about  $\epsilon$ , and  $\ell$  is the mean free path from Section 5.2. We will discuss higher energy considerations later in this section.

$W$  can be determined experimentally by observing the broadening of a step function profile, i.e., an abrupt change in concentration. The step function broadens into an erf profile with a 10% to 90% width of  $3.6 W$ , as illustrated in Fig. 26.

From diffusion theory, we also know that, if the original profile is a Gaussian or an erf described by  $Dt_0$ , the diffused profile is also a Gaussian or erf described by  $Dt_M = Dt_0 + Dt$ . Similarly, in a sputter profiling experiment, if the original profile is described by the parameter  $W_0$ , the measured profile will be described by  $W_M = \sqrt{W_0^2 + W^2}$ . Thus, the profile broadens in rms fashion.

#### 5.4.3 Experiment

We have performed ASP experiments [19] to examine the broadening of the Si-SiO<sub>2</sub> interface as a function of ion energy for Ne<sup>+</sup> and Xe<sup>+</sup> bombardment. The experimental setup will be discussed in Section 6. The measured sputtering yields of SiO<sub>2</sub> are shown in Fig. 27. The solid curves are obtained from our sputtering model with SiO<sub>2</sub> treated as a lattice of Ne atoms and with  $E_d = 25$  eV. Neon, with an atomic mass of 20, has a suitable average



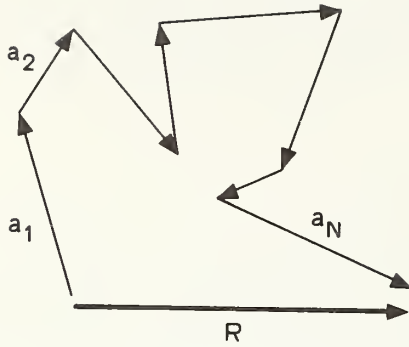


Fig. 25. Schematic illustration of a random walk with  $N$  steps of lengths  $a_1$  and a net distance traveled  $R$ .  $R^2 = Na^2$ .

mass for  $\text{SiO}_2$ . The sputtering curve for  $\text{Ne}^+$  bombardment fits the data quite well. This may be due to the fact that the incorporation of Ne atoms into the  $\text{SiO}_2$  lattice does not affect its average mass. The measured yields for  $\text{Ar}^+$  and  $\text{Xe}^+$  are larger than predicted by the model at low energies. This may result from a larger incorporation of noble gas atoms at low sputtering yields, which makes the lattice effectively heavier. The range of the incoming ions is thereby reduced, more energy is released near the specimen surface, and the sputtering yield increases.

The measured interface widths are plotted in Fig. 28. The solid curves are calculated from the mixing model with an assumed original 10% to 90% interface width of  $3.6 W_0 = 2.0 \text{ nm}$  and with  $(\overline{a^2})^{1/2} = a_{\text{rms}} = 0.33 \text{ nm}$ . The divergence of the solid curves from the data at high energies is due to the increase of  $a_{\text{rms}}$  with energy. The dashed curves are a higher energy approximation which we discuss in the next section. If the value of  $3.6 W_0$  is increased beyond 2.0 nm, the curves in Fig. 28 will move closer together. Thus, at a particular ion energy, the different broadening parameters obtained for  $\text{Ne}^+$ ,  $\text{Ar}^+$ , and  $\text{Xe}^+$  provide good evidence for the actual interface width. Figure 28 illustrates that the mixing model is entirely consistent with the measured interface widths.

#### 5.4.4 Extension to Higher Energies

At energies greater than 1 keV, Eq. (66) must be used to evaluate  $\overline{a^2}$ . In that equation,  $\ell(\epsilon)$  is the mean free path between collisions which we discussed in the second section of this chapter. We determined there, in Eqs. (22) and (26), that, as a first approximation,

$$\ell(\epsilon) \approx \gamma k \epsilon = k \epsilon \quad (67)$$

where  $\gamma$  and  $k$  are as defined in Eqs. (23) and (27). Note that  $\gamma$  and  $k$  refer to the atom of interest, a dopant atom, for example, striking a lattice atom and do not depend on the incident ion.

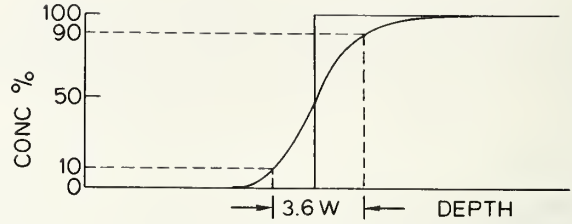


Fig. 26. A step function concentration profile is broadened by ion knock-on mixing into an erf profile with a 10% to 90% width of  $3.6 W$ .

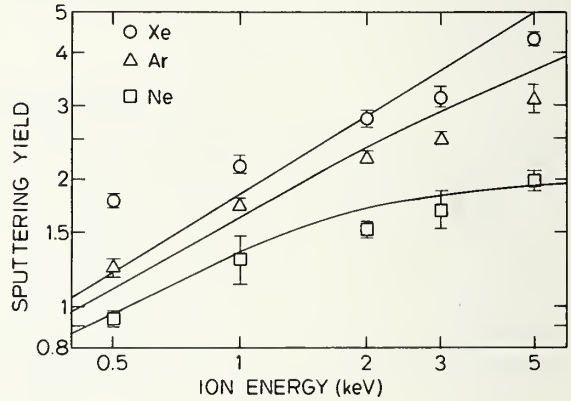


Fig. 27. Average and standard deviation of sputtering yields (atoms/ion) in thermal  $\text{SiO}_2$  as a function of ion energy for  $\text{Ne}^+$ ,  $\text{Ar}^+$ , and  $\text{Xe}^+$  bombardment. Solid curves are the predictions of our sputtering model for a lattice of Ne atoms (similar mass).



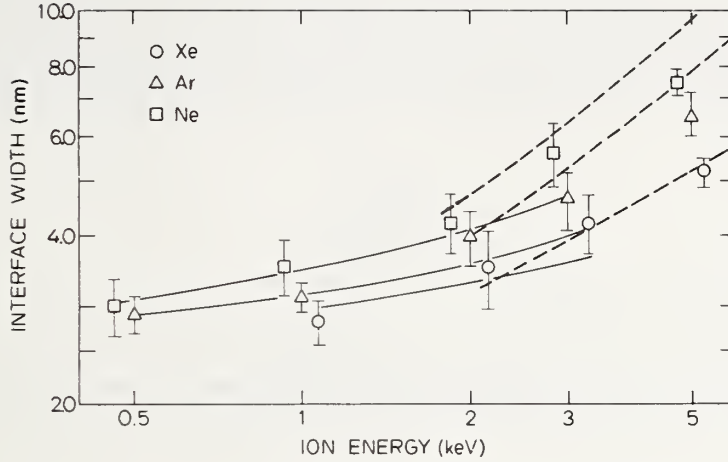


Fig. 28. Average and standard deviation of the measured 10% to 90% Si-SiO<sub>2</sub> interface widths as a function of ion energy for Ne<sup>+</sup>, Ar<sup>+</sup>, and Xe<sup>+</sup> bombardment. Solid curves are the low energy predictions of our mixing model for an original interface width of 2 nm. Dashed curves are predicted by the high energy formula for W.

$N(\epsilon) d\epsilon$ , the number of collisions occurring between  $\epsilon$  and  $\epsilon + d\epsilon$ , may be roughly approximated as follows. Suppose that an ion of energy  $E_0$  collides with a lattice atom, producing two atoms of energy  $E_0/2$  which then collide to produce four atoms of energy  $E_0/4$  and so on. For such a process,  $N(\epsilon) \propto 1/\epsilon^2$ . Eventually, there will be  $E_0/2E_d$  atoms with average energy  $2E_d$  (recall the Kinchin-Pease formula) at which point no further displacements occur. In Eq. (66), we will use  $2E_d$  as the lower limit of integration. We will also use  $\gamma_i E_0$  as the upper limit since  $\gamma_i E_0$  is the maximum energy that can be transferred to a lattice atom by the incident ion. We now choose

$$N(\epsilon) = 2E_0/\epsilon^2 \quad (68)$$

so that

$$\int N(\epsilon) d\epsilon \cong \int_{2E_d}^{\gamma_i E_0} \frac{2E_0}{\epsilon^2} d\epsilon \cong \frac{E_0}{E_d}. \quad (69)$$

Recall that  $E_0/E_d$  is the number of collisions that occurred in the solid. Equation (66) may now be written as follows:

$$\overline{a^2} = \frac{E_d}{E_0} \int_{2E_d}^{\gamma_i E_0} (\kappa\epsilon)^2 \frac{2E_0}{\epsilon^2} d\epsilon \cong 2\gamma_i \kappa^2 E_d E_0. \quad (70)$$

Substituting this value of  $\overline{a^2}$  into Eq. (65), we obtain the following appealing result:

$$W^2 = \frac{\gamma_i \kappa^2 E_0 E}{3S}. \quad (71)$$

$E_d$  has cancelled out of the equation. Ishitani and Shimizu [32] point out that, at these higher ion energies, the parameter  $E_d$  does not affect the broadening since low energy collisions (a few  $E_d$ ) become unimportant.

At this point, we pause to consider the applicability of this equation. Clearly, the assumptions made above are of a very approximate nature. As the ion energy increases, the form of  $N(\epsilon) \propto 1/\epsilon^2$ , which we have used, becomes inaccurate. The number of high energy collisions is exaggerated due, in part, to the electronic energy losses at higher energies. We see that Eq. (71) is only applicable when the electronic energy loss is small. We may, as a further simplification, let the energy of the ion  $E_0$  equal the nuclear energy loss  $E$  in Eq. (71). Thus,

$$W^2 = \frac{\gamma_1 (KE)^2}{3S} \quad (72)$$

Our assumptions also break down when the mass of the dopant atom of interest differs significantly from the mass of a lattice atom.

Equation (72) can only be expected to indicate trends with energy or sputtering yield and to roughly predict the broadening. We will demonstrate that Eq. (72) yields reasonable agreement with Monte Carlo calculations and experimental data. As a zeroeth-order approximation, then, Eq. (72) is justified by its utility and its simplicity.

Table 3a  
COMPARISON OF MONTE CARLO CALCULATIONS [32] OF  
THE BROADENING INDUCED BY  $Ar^+$  BOMBARDMENT OF Si  
WITH THE PREDICTIONS OF THE PRESENT MODEL

$Ar^+ \rightarrow Si$		Broadening Parameters (nm)			
		5 keV		10 keV	
Angle $\theta$	Poten- tial	Monte Carlo	$2.4 \sqrt{W}$	Monte Carlo	$2.4 \sqrt{W}$
0°	LJ	14.0	9.1	26.0	16.4
0°	TF	8.0	6.9	14.0	12.3
60°	LJ	9.0	5.5	15.0	8.9
60°	TF	6.0	4.0	10.0	7.6

Table 3b

Ratios		Monte Carlo	$2.4 \sqrt{W}$
$\frac{10 \text{ keV}}{5 \text{ keV}}$	0° LJ	1.9	1.8
	60°	1.7	1.6
	0° TF	1.8	1.8
	60°	1.7	1.9
$\frac{60^\circ}{60^\circ}$	5 keV LJ	1.6	1.7
	10 keV	1.7	1.8
	5 keV TF	1.3	1.7
	10 keV	1.4	1.6

Ishitani and Shimizu [32] have performed Monte Carlo calculations for 5 and 10 keV Ar<sup>+</sup> bombardment of silicon at 0° and 60° incidence. In their paper, they tabulate the nuclear energy loss  $E$ , the sputtering yield  $S$ , and the damage yield which conforms fairly well to the Kinchin-Pease formula. They also examine the broadening of a step function profile of tagged Si atoms and tabulate the 20% to 80% width of the broadened profile. Their results are ideally suited for a comparison with Eq. (72).

For the interaction of lattice atoms, the expression for  $K$  from Eqs. (27) and (67) reduces to

$$K = \frac{0.0051}{nZ^{5/3}} \text{ nm eV}^{-1} . \quad (73)$$

For Si,  $K = 0.012$ .  $\gamma = 0.97$  for Ar<sup>+</sup> incident on Si. The 20% to 80% width of an erf profile is 2.4  $W$ . Results are shown in Table 3a for the two potentials, Lenz-Jensen (LJ) and Thomas-Fermi, considered in the Monte Carlo calculations [32]. The magnitudes of broadening compare favorably. In particular, the trends with energy and angle predicted by Eq. (72) agree well with the Monte Carlo calculations, as shown in Table 3b.

Finally, we return again to our Si-SiO<sub>2</sub> data from Fig. 28. We apply Eq. (72) with the value of  $K = 0.012$  previously calculated for Si. We also use the measured sputtering yields of Fig. 27 and again assume that the original interface width is 2.0 nm. The results are shown as dashed lines in Fig. 28. The energy and ion dependence is quite reasonable. The accurate prediction of the magnitude of the broadening is somewhat fortuitous.

#### 5.4.5 Summary

We have developed a simple model of ion knock-on broadening based on an analogy to thermal diffusion theory. Broadening occurs in rms fashion, i.e.,

$$W_M = \sqrt{W_0^2 + W^2} \quad (74)$$

where  $W_0$  is an unperturbed width and  $W$  is the broadening parameter.

At low energies, ( $E \lesssim 1$  keV), we obtained

$$W^2 = \frac{Ea^2}{6E_d S} \quad (75)$$

where  $a$  is the nearest neighbor distance in the solid. The energy dependence of  $W$  is seen to be quite weak (as  $E$  increases, so does  $S$ ). The sputtering yield dependence indicates that, for two different bombarding ions of the same energy,

$$\frac{W_1^2}{W_2^2} = \frac{S_2}{S_1} . \quad (76)$$

At higher energies ( $1 \text{ keV} \lesssim E \lesssim 10 \text{ keV}$ ), provided that the electronic energy losses of the incident ion and of the lattice or dopant atoms are small, we used the following semi-empirical formula:

$$W^2 = \frac{\gamma_i (KE)^2}{3S} . \quad (77)$$

Comparisons with Monte Carlo calculations and with an ASP experiment performed on the Si-SiO<sub>2</sub> interface produced reasonable agreement.

## 6. EXPERIMENTAL METHODS IN ASP STUDIES OF THE Si-SiO<sub>2</sub> INTERFACE

### 6.1 Introduction

We have referred throughout this report to ASP studies of the Si-SiO<sub>2</sub> interface performed in our laboratory. In this chapter, we examine the experimental technique used in these studies.

In Section 6.2, we reiterate the various physical mechanisms affecting the measurement and describe how these are dealt with experimentally. In Section 6.3, electron stimulated desorption of oxygen from SiO<sub>2</sub> is discussed. In Section 6.4, the specific experimental procedure for the Si-SiO<sub>2</sub> interface studies is outlined. Finally, the crater-edge profiling technique is briefly described in Section 6.5.

### 6.2 Experimental Suppression of Profile Broadening

We have mentioned, in the previous chapters, several mechanisms which affect the measured Auger profile. The most important mechanisms that broaden the profiles are listed here. An experimental response to each of these mechanisms is then presented in sequence.

- |                                    |                             |
|------------------------------------|-----------------------------|
| (1) electron escape depth          | (5) preferential sputtering |
| (2) ion knock-on mixing            | (6) ion-induced roughness   |
| (3) electron stimulated desorption | (7) charging                |
| (4) gas readsorption               |                             |

- (1) Electron escape depth: We dealt with this effect in Chapter 4. Optimum depth resolution is obtained if the escape depth is minimized. The Si<sub>LV</sub> (92 eV) peak is conveniently located at the minimum of escape depth.
- (2) Ion knock-on mixing: We examined this effect in Chapter 5. Broadening is minimized by using low energy ions striking the specimen at acute angles of incidence.
- (3) Electron stimulated desorption: As we discuss in the next section, the electron flux must be kept at an appropriately low level so that the oxygen level in SiO<sub>2</sub> does not decrease perceptibly. The use of electron energies above about 3 keV is necessary to do this.
- (4) Gas readsorption: In our sputtering experiments, the chamber is backfilled with the sputtering gas with the ion pump off. Sputtered atoms may continue to circulate in the chamber, and desorption from other parts of the chamber occurs. These background constituents may then be readsorbed. Oxygen, for example, sticks to a free Si surface but not to SiO<sub>2</sub>. Thus, broadening of the Si-SiO<sub>2</sub> interface width may occur if the rate of O readsorption is significant in comparison to the sputtering rate. This effect is countered by using a large sputtering rate and by sputtering with Ne in conjunction with a liquid nitrogen cryopanel. Xe and Ar will condense on the cryopanel and, therefore, cannot be used.
- (5) Preferential sputtering: In a multicomponent specimen, one species may sputter preferentially, thereby altering the relative surface concentrations. This effect may depend on the energy and mass of the incident ion. Experimental evidence indicates that preferential sputtering does not occur in thermal SiO<sub>2</sub>.
- (6) Ion-induced roughness: This effect was examined in Chapter 4. The ion beam is rastered to ensure that the crater is virtually flat over the width of the electron beam. A TV raster could produce unwanted ridges; therefore, a pseudorandom raster was used at energies <3 keV. At 5 keV, a broad beam with slight TV rastering was used. When the width of the beam is much greater than the raster spacing, roughness is minimized.



- (7) Charging: We find that thin  $\text{SiO}_2$  layers, although they are insulating, do not charge significantly ( $<1$  eV) if good contact is made to the surface by copper clips and to the back surface by a metallic tray. Specimens in which charging did occur due to poor contact were abandoned.

### 6.3 Electron Stimulated Desorption [13]

It is well known that  $\text{SiO}_2$  decomposes under prolonged electron irradiation [43]. The most pronounced beam interaction effect is dissociation and subsequent desorption of oxygen. This results in time-dependent changes in the amplitudes of the Auger spectra of oxygen, as shown in Fig. 29. In the upper part of Fig. 29, we show how oxygen is depleted from the

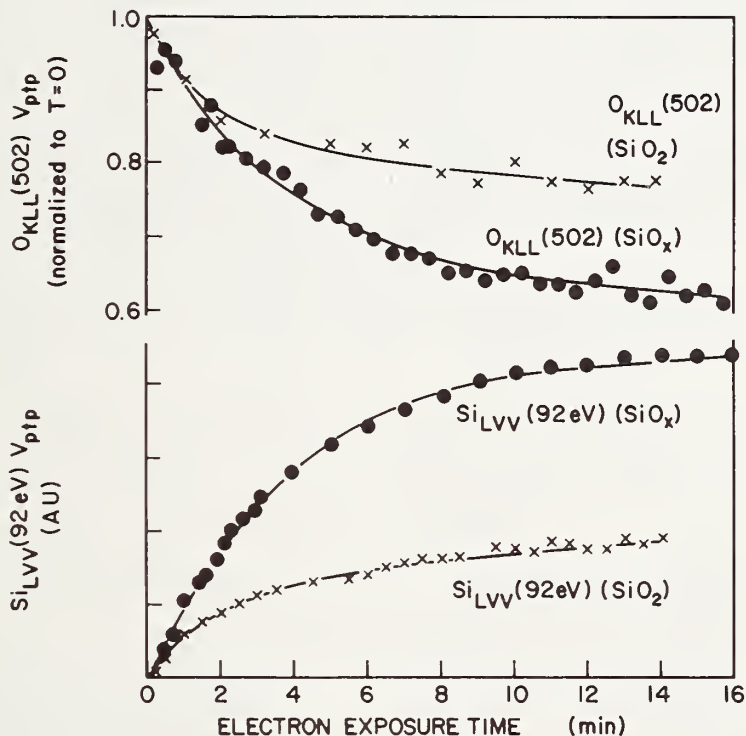


Fig. 29. The effect of ESD on the  $\text{O}_{\text{KLL}}$  and  $\text{Si}_{\text{LVV}}$  (92 eV) lines from  $\text{SiO}_2$  and  $\text{SiO}_x$  ( $x = 1.4$ ) shown as a function of irradiation time for an electron beam flux larger than  $2 \times 10^{17} \text{ cm}^{-2} \text{ s}^{-1}$  at 2 keV.

surface of  $\text{SiO}_2$  and  $\text{SiO}_x$ , where  $x = 1.4$ . Note that the initial rate is the same for the two specimens but that more oxygen is desorbed from the unsaturated oxide ( $x = 1.4$ ) at long irradiation times. This is a general feature. The smaller the stoichiometry factor  $x$ , the more volatile the specimen appears to be under electron irradiation, provided the specimen has been exposed to normal atmosphere (e.g., "as-received" virgin sample). Depletion of oxygen from the surface of the specimens is accompanied by a growth of the elemental silicon LVV line at 92 eV, as shown in the lower part of Fig. 29. Prior to electron irradiation of the specimens ( $t = 0$ ), there is no "free" silicon even though we know that there is excess silicon in unsaturated oxides [44]. The reason for this is, of course, that the specimens have been exposed to atmosphere, and hence the specimens are oxidized to a depth sufficient to mask their bulk stoichiometry. Figure 29 is a typical example of excess irradiation at a primary electron flux larger than  $2 \times 10^{17} \text{ cm}^{-2} \text{ sec}^{-1}$  at 2 keV. We have investigated the effect of primary beam flux and energy on the interaction with silicon oxide surfaces in



terms of a desorption cross section of oxygen. The desorption cross section  $\sigma$  is related to the primary electron flux  $\Phi$  ( $\text{cm}^{-2} \text{s}^{-1}$ ) and defined by

$$\sigma = - \frac{1}{\Phi} \left( \frac{1}{V_{\text{ptp}}} \frac{d}{dt} (V_{\text{ptp}}) \right) \bigg|_{t=0} \quad (79)$$

where  $V_{\text{ptp}}$  is the  $O_{\text{KLL}}$  peak-to-peak height and  $t$  is the irradiation time. Both  $\Phi$  and  $V_{\text{ptp}}$  are experimentally obtainable quantities. The flux has been varied by rastering the beam over a known sample area. The rastering is done at a vertical frequency of 60 Hz and a horizontal frequency of 15750 Hz. In Fig. 30, we show how the cross section of Eq. (79) depends on the electron flux at 2 keV. Below  $2 \times 10^{17} \text{ cm}^{-2} \text{s}^{-1}$ , the cross section appears to be a well-defined quantity. At larger values of  $\Phi$ , the cross section increases rapidly, probably due to thermal enhancement of the desorption process. The magnitude of the total desorption cross section we observed,  $2 \times 10^{-21} \text{ cm}^2$  for oxygen, is in reasonable agreement with oxygen desorption from metal oxides such as SrO and MgO [45] where dissociation is a part of the process. The desorption cross section is also a function of the primary beam energy as shown in the upper part of Fig. 31. The linear relation is probably fortuitous. However, the important thing to note is that  $\sigma$  decreases with increasing energy to a small but finite value at higher energies. The reason for this energy dependence is to be found in the energy dependence of the secondary electron energy distribution. We have measured the secondary electron yield in the energy range 15 to 150 eV and 15 to 500 eV, as a function of primary electron energy. The result is shown in the lower part of Fig. 31. The total incident current was kept constant at 5  $\mu\text{A}$ . The fact that the number of secondary electrons in the given energy intervals decreases with increasing primary energy leads to a smaller number of ionized oxygen atoms in the surface region of the sample and, hence, to a yet smaller number of desorbed oxygen atoms. This desorption mechanism is elaborated on in the literature [45].

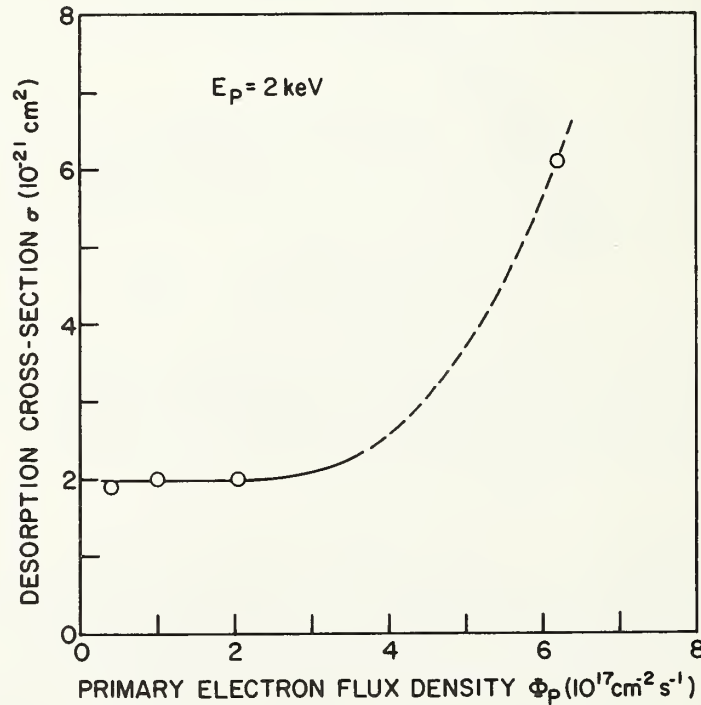


Fig. 30. The total desorption cross section of oxygen at 2 keV shown as a function of primary flux for a silicon oxide.

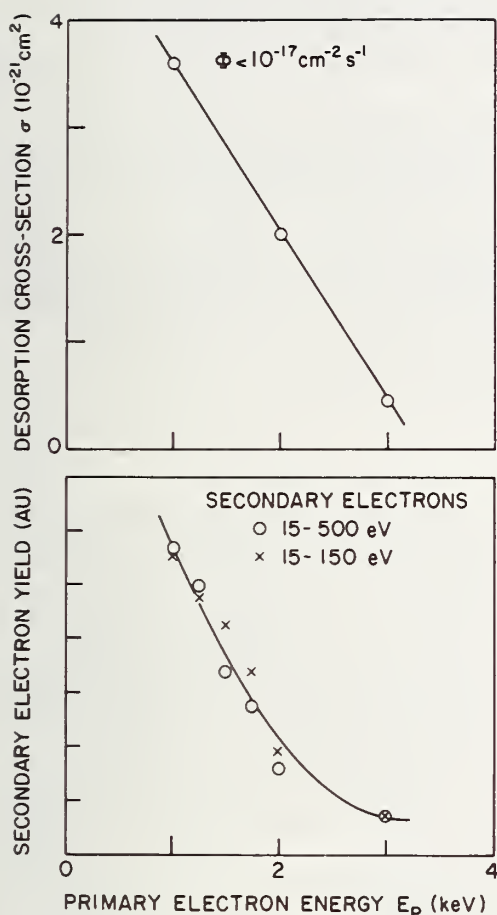


Fig. 31. The upper part shows the dependence of the cross section on primary electron energy; the lower part shows how the secondary electron density depends on primary electron energy. The secondary electron energies are given in the figure.

dom beam raster was used. The random raster minimized surface roughening. At 5 keV ion energies, a 3M model 430 ion gun was used. A large spot size with little or no line rastering again minimized any surface roughening which might occur. Experimental comparisons between the guns were made at 3 keV with consistent results. The chamber was backfilled to a pressure of  $\sim 5 \times 10^{-5}$  Torr with either Ne, Ar, or Xe. In all cases, ion current densities of  $22.2 \mu\text{A}/\text{cm}^2$  were used. Ion beam profiles were measured with a Faraday probe.

When the sputtering rate is too low ( $< 1 \text{ nm}/\text{min}$ ), oxygen readsorption can affect the measured interface width. Due to the low ionization probability for Xe, insufficient ion current was obtained at 500 eV to establish a reasonable sputtering rate. The readsorption effect was negligible in all other cases. A liquid nitrogen trap was used with the neon runs to minimize the  $\text{O}_2$  partial pressure.

A  $1\text{-}\mu\text{A}$  4.5-keV electron beam rastered over a  $200 \mu\text{m}$  by  $200 \mu\text{m}$  square was directed to the center of the sputtered crater. With these parameters, electron stimulated desorption of oxygen was negligible [13]. The ion beam was, in all cases, uniform to within 0.5% over the  $200 \mu\text{m}$  by  $200 \mu\text{m}$  square.

We conclude that the primary electron beam interactions in AES analysis depend on the chemical composition of the specimen under investigation and its previous history. Beam interactions may be minimized by a suitable choice of primary beam parameters such as energy and flux. We have found that at 2 keV a total electron exposure of less than  $10^{19} \text{ cm}^{-2}$  leaves the surface of silicon oxides, practically speaking, virgin insofar as the AES measurement is concerned.

In depth profiling work, we typically have applied a 4.5 keV rastered primary electron beam. The beam diameter is approximately  $10 \mu\text{m}$ , and the scanned area is typically  $10^{-4} \text{ cm}^2$ . With a total beam current of  $1 \mu\text{A}$ , we stay well below the exposure level that gives rise to noticeable oxygen desorption. We feel that the rastered primary electron beam is a necessary precaution in high-resolution AES work. It provides a uniform current density without deteriorating the signal-to-noise ratio.

#### 6.4 Experimental Procedure

The specimens used in our investigation were pieces from a single lightly doped Si (100) wafer oxidized at  $1000^\circ\text{C}$  for 40 min in dry  $\text{O}_2$  with a 5 min preanneal and postanneal in  $\text{N}_2$ . The oxide thickness was measured ellipsometrically and determined to be  $440 \pm 2 \text{ nm}$ .

The profiling experiments were performed in an Auger spectrometer at base pressures of  $\sim 10^{-9}$  Torr. Electrons from the integral gun of the cylindrical mirror analyzer struck the specimen surface at an angle of  $30^\circ$  to the surface normal. The angle of incidence of the ion beam was  $49^\circ$ .

Sputtering was performed with two different ion guns. For ion energies of 3 keV or less, a Varian ion gun with a pseudorange

The Si<sub>L<sub>LV</sub></sub> (92 eV) and O<sub>K<sub>LL</sub></sub> (502 eV) peak-to-peak heights were monitored during the experiments. The 92 eV Si peak appears only for Si atoms which are not bonded to oxygen. The escape depth minimum of ~0.5 nm occurs near 92 eV. In Chapter 4, we discussed an electron escape depth deconvolution technique [49] and showed that, for the detector geometry in our apparatus, the escape depth broadening is less than 0.3 nm for measured interface widths greater than 2.5 nm. Ten to ninety percent interface widths were measured for the Si 92 eV profile.

Further evidence for the absence of extraneous broadening effects comes from similar experiments in our laboratory. We have shown that the effect of sputtering nonuniformities on measured interface widths is less 0.5% of the oxide thickness for oxides as thick as 500 nm [46]. This corresponds in the present case to an error of less than 0.3 nm.

The interface width measurements assume a constant sputtering rate (nm/min) through the interfacial region. Sputtering rates for SiO<sub>2</sub> were determined from the time taken to reach the interface. The Si sputtering rate was measured for Ar<sup>+</sup> bombardment at 1 keV by masking one side of the oxide specimen, sputtering the other side well onto the Si, and measuring the sputtered depth with a Tencor Alpha-Step stylus apparatus. The Si sputtering rate measured in this manner was 5% less than the corresponding rate for SiO<sub>2</sub>.

## 6.5 Crater-Edge Profiling [1]

Ideally, sputtering produces a crater on the specimen of interest which is flat in the center and slopes upward away from the center. A crater formed on a thermal oxide of Si is schematically illustrated [47] in Fig. 32. A depth profile may be obtained by scanning an electron beam across the surface of the crater edge. The slope of the crater depends on the thickness of the oxide sputtered away. For a 100-nm thick oxide, a 5-nm depth profile may be obtained by sweeping the electron beam over a width of ~1 mm. The resolution of this technique deteriorates if the electron beam is wider than the lateral distance corresponding to an exposed depth of one escape depth. Escape depth considerations were discussed in Chapter 4. Escape depth deconvolution also proceeds as in Chapter 4.

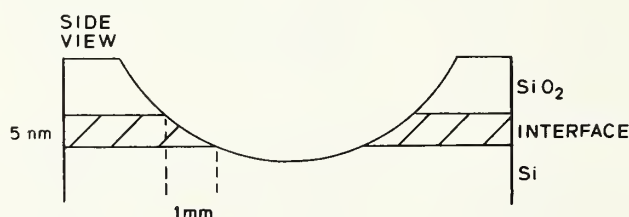


Fig. 32. Schematic illustration of the crater formed by sputtering a thin layer of SiO<sub>2</sub> on Si. From W. E. Spicer et al. [47].

In the Varian 2730 Auger spectrometer, the electron beam is electronically swept along the path of interest. This steady sweep of the intensely focused beam reduces electron stimulated desorption problems.

The crater-edge technique bears a strong resemblance to conventional angle lapping techniques; however, the angle involved is three orders of magnitude less. Once the crater is formed, the experimenter can return to it at leisure and perform many sweeps, thereby improving the signal-to-noise ratio.

The depth scale of the crater edge profile can be calibrated in two ways. If the ion beam profile is accurately known, the slope of the crater can be calculated. Otherwise, a normal ASP profile can be obtained as the crater is formed. The crater edge profile can then be compared to the normal profile for depth scale calibration. Further experiments can then be performed to investigate dopant distributions, etc. We have used this method [8] to examine phosphorus pileup at the Si-SiO<sub>2</sub> interface.

## 6.6 Experimental Results for the Width of the Si-SiO<sub>2</sub> Interface [46]

As an example of the capabilities of the ASP technique, we will now discuss experimental measurements of elemental and chemical profiles of silicon and oxygen in passing through the Si-SiO<sub>2</sub> interface. Specimens were prepared in a similar manner, as discussed in Section 6.4, except that growth times were varied to obtain specimens with thicknesses from 25 to 100 nm.

The strength of the elemental silicon LVV transition at 92 eV and the oxygen KLL transition at 510 eV were measured during the sputter profiling experiment. The silicon 92 eV transition is characteristic of silicon atoms bonded to other silicon atoms as in elemental silicon. Silicon atoms coordinated differently, such as in SiO<sub>2</sub> with each silicon atom bonded to four oxygen atoms, have different characteristic transition energies and line shapes, (78 eV for SiO<sub>2</sub>, for example) so that by monitoring the 92 eV transition, an accurate profile of the elemental silicon can be obtained.

Table 4

OXIDE THICKNESS DEPENDENCE OF THE WIDTH OF THE Si-SiO<sub>2</sub> TRANSITION REGION

Sample	W <sub>O</sub>	W <sub>Si</sub>
24 nm	3.16 nm	2.37 nm
24 nm	3.90 nm	2.74 nm
29.5 nm	3.55 nm	2.50 nm
31.0 nm	3.20 nm	2.31 nm
31.0 nm	3.20 nm	2.45 nm
58.5 nm	3.30 nm	2.42 nm
95.5 nm	3.14 nm	2.58 nm
Average	3.35 ± 0.25 nm	2.5 ± 0.15 nm
Average corrected for escape depth	2.9 ± 0.5 nm	2.35 ± 0.25 nm

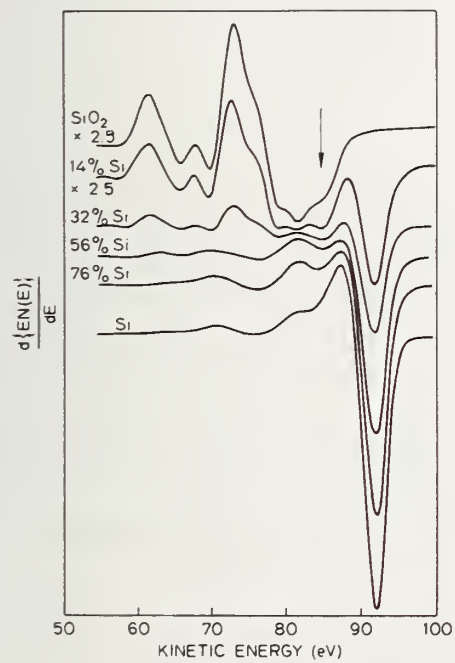


Fig. 33. Sequential Si<sub>LVV</sub> spectra obtained while sputtering through the Si-SiO<sub>2</sub> interface [46].

The width of the interface was taken as that distance over which this silicon 92 eV transition increased from 10% to 90% of its final value. For comparison purposes, the oxygen KLL profile was also measured, with the interface width defined in a similar way. Data from the silicon KLL transition will not be discussed since, with about a 3 nm escape depth, the minimum interface width observable with this transition is about 5 nm.

A typical profile is shown in Fig. 7 (Chapter 4) where the peak-to-peak heights of the Si LVV and oxygen KLL transitions are shown as a function of depth for the 100 nm oxide sample. A set of Si LVV spectra corresponding to such a profile is shown in Fig. 33.



In Table 4, we show measured interface width as a function of oxide thickness for oxides grown at 1000°C. The interface widths are remarkably similar, the average values being shown in the bottom row.

The 10% to 90% width of the interface is about 2.5 nm as determined by the Si LVV transition and 3.3 nm as determined by the oxygen KLL transition. There are three factors that may be responsible for the apparent discrepancy between the two values for interface width: escape depth, preferential ion knock-on effects, and the presence of an oxygen-containing phase of silicon at the interface other than SiO<sub>2</sub>.

Correcting the data for electron escape depth, we find that the values for interface width are 2.35 nm for the Si LVV and 2.9 nm for the oxygen KLL. Although escape depth is certainly contributing to the discrepancy, the corrected values for interface width are outside the limits of experimental error. The difference in interface width is therefore probably related to preferential knock-on effects or the presence of an additional oxygen-containing phase of silicon.

An estimate of the limit of any additional broadening contribution that might be proportional to thickness can be obtained by dividing the rms deviation, 0.15 nm, by the average oxide thickness of the samples, ~40 nm. This gives an upper limit of 0.4% for broadening proportional to oxide thickness. This value is the level at which contributions from the nonflat sputtering crater bottom must be taken into consideration and probably represents the limit of present capabilities. (Note, however, this would give an ~4 nm interface width for a 1-μm thick oxide and an abrupt interface.)

#### REFERENCES

1. N. J. Taylor, J. S. Johannessen, and W. E. Spicer, Crater-Edge Profiling in Interface Analysis Employing Ion Beam Etching and AES, *Appl. Phys. Letts.* 29, 497-499 (1976).
2. C. J. Powell, Attenuation Lengths of Low-Energy Electrons in Solids, *Surf. Sci.* 44 29-46 (1974).
3. H. J. Fitting, H. Glaefke, and W. Wild, Attenuation Length and Escape Depth of Excited Electrons in Solids, *Surf. Sci.* 75, 267-278 (1978).
4. I. Lindau and W. E. Spicer, The Probing Depth in Photoemission and Auger-Electron Spectroscopy, *J. Electron Spectrosc. and Rel. Phen.* 3, 409-413 (1974).
5. D. P. Woodruff, Surface Structure from Angular Dependence of Auger Electron Emission, *Surf. Sci.* 53, 538-545 (1975).
6. D. Bohm and D. Pines, A Collective Description of Electron Interactions: III. Coulomb Interactions in a Degenerate Electron Gas, *Phys. Rev.* 92, 609-625 (1953).
7. D. R. Penn, Electron Attenuation Lengths for Free-Electron Metals, *J. Vac. Sci. Technol.* 13, 221-223 (1976).
8. S. A. Schwarz, C. R. Helms, W. E. Spicer, and N. J. Taylor, High Resolution Auger Sputter Profiling Study of the Effect of Phosphorus Pileup on the Si-SiO<sub>2</sub> Interface Morphology, *J. Vac. Sci. Technol.* 15, 227-230 (1978).
9. H. Iwasaki and S. Nakamura, On the Depth Profiles by ESCA, *Surf. Sci.* 57, 779-780 (1976).
10. T. E. Gallon, A Simple Model for the Dependence of Auger Intensities on Specimen Thickness, *Surf. Sci.* 17, 486-489 (1969).
11. C. R. Helms, W. E. Spicer, and N. M. Johnson, New Studies of the Si-SiO<sub>2</sub> Interface Using Auger Sputter Profiling, *Solid State Commun.* 25, 673-676 (1978).<sup>2</sup>



12. R. Flitsch and S. I. Raider, Electron Mean Escape Depths from X-ray Photoelectron Spectra of Thermally Oxidized Silicon Dioxide Films on Silicon, *J. Vac. Sci. Technol.* 12, 305-308 (1975).
13. J. S. Johannessen, W. E. Spicer, and Y. E. Strausser, An Auger Analysis of the SiO<sub>2</sub>-Si Interface, *J. Appl. Phys.* 47, 3028-3037 (1976).
14. J. S. Johannessen, C. R. Helms, W. E. Spicer, and Y. E. Strausser, Auger Depth Profiling of MNOS Structures by Ion Sputtering, *IEEE Trans. Electron Devices* ED-24, 547-551 (1977).
15. C. R. Helms, Y. E. Strausser, and W. E. Spicer, Observation of an Intermediate Chemical State of Silicon in the Si-SiO<sub>2</sub> Interface by Auger Sputter Profiling, *Appl. Phys.* 33, 767-760 (1978).
16. J. W. Coburn, Sputtering in the Surface Analysis of Solids: A Discussion of Some Problems, *J. Vac. Sci. Technol.* 13, 1037-1044 (1976).
17. D. M. Smith and T. E. Gallon, Auger Emission from Solids: The Estimation of Backscattering Effects and Ionization Cross Sections, *J. Phys. D: Appl. Phys.* 7, 151-161 (1974).
18. S. A. Schwarz and C. R. Helms, A Statistical Model of Sputtering, submitted to *J. Appl. Phys.* 50, 5492-5499 (1979).
19. S. A. Schwarz and C. R. Helms, Model of Ion Knock-On Mixing with Application to Si-SiO<sub>2</sub> Interface Studies, *J. Vac. Sci. Technol.* 16, 781-783 (1979).
20. G. Carter and J. S. Colligon, *Ion Bombardment of Solids*, Elsevier Publishing Co., New York, 1968.
21. J. F. Gibbons, Ion Implantation in Semiconductors--Part I: Range Distribution Theory and Experiments, *Proc. IEEE* 56, 295-319 (1968).
22. O. B. Firsov, A Qualitative Interpretation of the Mean Electron Excitation Energy in Atomic Collisions, *J. Exper. Theoret. Phys. (USSR)* 36, 1517-1523 (1959).
23. G. H. Kinchin and R. S. Pease, The Displacement of Atoms in Solids by Radiation, *Rep. Progr. Phys.* 18, 2-50 (1955).
24. J. F. Gibbons, Ion Implantation in Semiconductors--Part II: Damage Production and Annealing, *Proc. IEEE* 60, 1062-1096 (1972).
25. N. Bohr, The Penetration of Atomic Particles through Matter, *Mat. Fys. Medd. Dan. Vid. Selsk.* 18, 1-144 (1941).
26. R. M. Eisberg, *Fundamentals of Modern Physics* (John Wiley and Sons, Inc., New York, 1961).
27. L. B. Loeb, *The Kinetic Theory of Gases* (Dover Publications, Inc., New York, 1961).
28. J. Lindhard, M. Scharff, and H. Schiott, Range Concepts and Heavy Ion Ranges, *Mat. Fys. Medd. Dan. Vid. Selsk.* 33, 1-39 (1963).
29. J. Lindhard and M. Scharff, Energy Dissipation by Ions in the keV Region, *Phys. Rev.* 124, 128-130 (1961).
30. J. Lindhard and A. Winther, Stopping Power of Electron Gas and Equipartition Rule, *Mat. Fys. Medd. Dan. Vid. Selsk.* 34, 1-21 (1964).
31. F. Seitz, On the Disordering of Solids by Action of Fast Massive Particles, *Disc. Farad. Soc.* 5, 271-282 (1949).

32. T. Ishitani and R. Shimizu, Computer Simulation of Atomic Mixing during Ion Bombardment, *Appl. Phys.* 6, 241-248 (1975).
33. P. Sigmund, Theory of Sputtering. I. Sputtering Yield of Amorphous and Polycrystalline Targets, *Phys. Rev.* 184, 383-416 (1969).
34. D. Rosenberg and G. K. Wehner, Sputtering Yields for Low Energy  $\text{He}^+$ ,  $\text{Kr}^+$ , and  $\text{Xe}^+$  Ion Bombardment, *J. Appl. Phys.* 33, 1842-1845 (1962).
35. E. P. EerNisse, Sputtering of Au by 45 keV Ions for Different Fluences, *Appl. Phys. Letts.* 29, 14-17 (1976).
36. P. K. Rol, J. M. Fluit, and J. Kistemaker, Sputtering of Copper by Bombardment with Ions of 5-25 keV, *Physica* 26, 1000-1011 (1960).
37. V. A. Molchanov and V. G. Tel'kovskii, Variation of the Cathode Sputtering Coefficient as a Function of the Angle of Incidence of Ions on a Target, *Sov. Phys. Doklady* 6, 137-138 (1961).
38. D. E. Harrison, Jr., P. W. Kelley, B. J. Garrison, and N. Winograd, Low Energy Ion Impact Phenomena on Single Crystal Surfaces, *Surf. Sci.* 76, 311-322 (1978).
39. H. G. Prival, A Model of the Ion Sputtering Process, *Surf. Sci.* 76, 443-463 (1978).
40. Prof. W. A. Harrison, Stanford University, private communication.
41. H. H. Andersen, The Depth Resolution of Sputter Profiling, *Appl. Phys.* 18, 131-140 (1979).
42. P. K. Haff and Z. E. Switkowski, Ion Beam-Induced Atomic Mixing, *J. Appl. Phys.* 48, 3383-3386 (1977).
43. S. Thomas, Electron-Irradiation Effect in the Auger Analysis of  $\text{SiO}_2$ , *J. Appl. Phys.* 45, 161-166 (1974).
44. J. S. Johannessen, W. E. Spicer, and Y. E. Strausser, Phase Separation in Silicon Oxides as Seen by Auger Electron Spectroscopy, *Appl. Phys. Letts.* 27, 452-454 (1975).
45. T. E. Madey and J. T. Yates, Electron-Stimulated Desorption as a Tool for Studies of Chemisorption: A Review, *J. Vac. Sci. Technol.* 8, 525-555 (1971).
46. C. R. Helms, N. M. Johnson, S. A. Schwarz, and W. E. Spicer, Auger Sputter Profiling Studies of the Si- $\text{SiO}_2$  Interface, *The Physics of  $\text{SiO}_2$  and Its Interfaces*, S. T. Pantalides, ed., pp. 366-372 (Pergamon Press, New York, 1978).
47. W. E. Spicer, I. Lindau, and C. R. Helms, *Frontiers in Surface and Interface Analysis, Res. Dev.* pp. 20-31 (Dec 1977).

U.S. DEPT. OF COMM. <b>BIBLIOGRAPHIC DATA SHEET</b> (See instructions)		1. PUBLICATION OR REPORT NO. SP 400-67	2. Performing Organ. Report No.	3. Publication Date September 1981
4. TITLE AND SUBTITLE <i>Semiconductor Measurement Technology: The Capabilities and Limitations of Auger Sputter Profiling for Studies of Semiconductors</i>				
5. AUTHOR(S) S. A. Schwarz, C. R. Helms, W. E. Spicer, and N. J. Taylor				
6. PERFORMING ORGANIZATION (If joint or other than NBS, see instructions)  Stanford University      Varian Associates Stanford, CA 94305      Palo Alto, CA 94303			7. Contract/Grant No.  8. Type of Report & Period Covered Final	
9. SPONSORING ORGANIZATION NAME AND COMPLETE ADDRESS (Street, City, State, ZIP) Defense Advanced Research Projects Agency      and the 1400 Wilson Boulevard      National Bureau of Standards Arlington, VA 22203      Washington, DC 20234				
10. SUPPLEMENTARY NOTES  Library of Congress Catalog Card Number: 81-600003  <input type="checkbox"/> Document describes a computer program; SF-185, FIPS Software Summary, is attached.				
11. ABSTRACT (A 200-word or less factual summary of most significant information. If document includes a significant bibliography or literature survey, mention it here)  Materials characterization is a critical area in current silicon integrated circuit technology. Those techniques that are commonly used include Auger sputter profiling, X-ray photoelectron spectroscopy, secondary ion mass spectrometry, and Rutherford backscattering. All of these techniques have unique capabilities and limitations for studies of silicon device structures. In this paper, we describe the capabilities and limitations of Auger sputter profiling especially with regard to sensitivity, spatial resolution, depth resolution, and chemical state determination. Although much of the discussion centers on Auger sputter profiling, the results are also applicable to X-ray photoelectron spectroscopy and secondary ion mass spectrometry.				
12. KEY WORDS (Six to twelve entries; alphabetical order; capitalize only proper names; and separate key words by semicolons) Auger electron spectroscopy (AES); metal-oxide-semiconductor (MOS), secondary ion mass spectrometry (SIMS); semiconductor devices; sputtering; X-ray photoelectron spectroscopy (XPS, ESCA).				
13. AVAILABILITY  <input checked="" type="checkbox"/> Unlimited <input type="checkbox"/> For Official Distribution. Do Not Release to NTIS <input type="checkbox"/> Order From Superintendent of Documents, U.S. Government Printing Office, Washington, D.C. 20402.  <input checked="" type="checkbox"/> Order From National Technical Information Service (NTIS), Springfield, VA. 22161			14. NO. OF PRINTED PAGES 53  15. Price	



Announcement of Semiconductor Measurement Technology  
List of Publications 72 — 1962-1980

Chief  
Electron Devices Division  
National Bureau of Standards  
Bldg. 225, Room A305  
Washington, DC 20234

Dear Sir:

Please send a copy of your latest "Semiconductor Measurement Technology,  
List of Publications 72."

Name \_\_\_\_\_

Company \_\_\_\_\_

Address \_\_\_\_\_

City \_\_\_\_\_ State \_\_\_\_\_ Zip Code \_\_\_\_\_





# NBS TECHNICAL PUBLICATIONS

## PERIODICALS

**JOURNAL OF RESEARCH**—The Journal of Research of the National Bureau of Standards reports NBS research and development in those disciplines of the physical and engineering sciences in which the Bureau is active. These include physics, chemistry, engineering, mathematics, and computer sciences. Papers cover a broad range of subjects, with major emphasis on measurement methodology and the basic technology underlying standardization. Also included from time to time are survey articles on topics closely related to the Bureau's technical and scientific programs. As a special service to subscribers each issue contains complete citations to all recent Bureau publications in both NBS and non-NBS media. Issued six times a year. Annual subscription: domestic \$13; foreign \$16.25. Single copy, \$3 domestic; \$3.75 foreign.

NOTE: The Journal was formerly published in two sections: Section A "Physics and Chemistry" and Section B "Mathematical Sciences."

**DIMENSIONS/NBS**—This monthly magazine is published to inform scientists, engineers, business and industry leaders, teachers, students, and consumers of the latest advances in science and technology, with primary emphasis on work at NBS. The magazine highlights and reviews such issues as energy research, fire protection, building technology, metric conversion, pollution abatement, health and safety, and consumer product performance. In addition, it reports the results of Bureau programs in measurement standards and techniques, properties of matter and materials, engineering standards and services, instrumentation, and automatic data processing. Annual subscription: domestic \$11; foreign \$13.75.

## NONPERIODICALS

**Monographs**—Major contributions to the technical literature on various subjects related to the Bureau's scientific and technical activities.

**Handbooks**—Recommended codes of engineering and industrial practice (including safety codes) developed in cooperation with interested industries, professional organizations, and regulatory bodies.

**Special Publications**—Include proceedings of conferences sponsored by NBS, NBS annual reports, and other special publications appropriate to this grouping such as wall charts, pocket cards, and bibliographies.

**Applied Mathematics Series**—Mathematical tables, manuals, and studies of special interest to physicists, engineers, chemists, biologists, mathematicians, computer programmers, and others engaged in scientific and technical work.

**National Standard Reference Data Series**—Provides quantitative data on the physical and chemical properties of materials, compiled from the world's literature and critically evaluated. Developed under a worldwide program coordinated by NBS under the authority of the National Standard Data Act (Public Law 90-396).

NOTE: The principal publication outlet for the foregoing data is the Journal of Physical and Chemical Reference Data (JPCRD) published quarterly for NBS by the American Chemical Society (ACS) and the American Institute of Physics (AIP). Subscriptions, reprints, and supplements available from ACS, 1155 Sixteenth St., NW, Washington, DC 20056.

**Building Science Series**—Disseminates technical information developed at the Bureau on building materials, components, systems, and whole structures. The series presents research results, test methods, and performance criteria related to the structural and environmental functions and the durability and safety characteristics of building elements and systems.

**Technical Notes**—Studies or reports which are complete in themselves but restrictive in their treatment of a subject. Analogous to monographs but not so comprehensive in scope or definitive in treatment of the subject area. Often serve as a vehicle for final reports of work performed at NBS under the sponsorship of other government agencies.

**Voluntary Product Standards**—Developed under procedures published by the Department of Commerce in Part 10, Title 15, of the Code of Federal Regulations. The standards establish nationally recognized requirements for products, and provide all concerned interests with a basis for common understanding of the characteristics of the products. NBS administers this program as a supplement to the activities of the private sector standardizing organizations.

**Consumer Information Series**—Practical information, based on NBS research and experience, covering areas of interest to the consumer. Easily understandable language and illustrations provide useful background knowledge for shopping in today's technological marketplace.

*Order the above NBS publications from: Superintendent of Documents, Government Printing Office, Washington, DC 20402.*

*Order the following NBS publications—FIPS and NBSIR's—from the National Technical Information Services, Springfield, VA 22161.*

**Federal Information Processing Standards Publications (FIPS PUB)**—Publications in this series collectively constitute the Federal Information Processing Standards Register. The Register serves as the official source of information in the Federal Government regarding standards issued by NBS pursuant to the Federal Property and Administrative Services Act of 1949 as amended, Public Law 89-306 (79 Stat. 1127), and as implemented by Executive Order 11717 (38 FR 12315, dated May 11, 1973) and Part 6 of Title 15 CFR (Code of Federal Regulations).

**NBS Interagency Reports (NBSIR)**—A special series of interim or final reports on work performed by NBS for outside sponsors (both government and non-government). In general, initial distribution is handled by the sponsor; public distribution is by the National Technical Information Services, Springfield, VA 22161, in paper copy or microfiche form.

**U.S. DEPARTMENT OF COMMERCE  
National Bureau of Standards**

Washington, DC 20234

POSTAGE AND FEES PAID  
U.S. DEPARTMENT OF COMMERCE  
COM-215



OFFICIAL BUSINESS

Penalty for Private Use, \$300

THIRD CLASS  
BULK RATE

---